

# A New Aerial Approach for Quantifying and Attributing Methane Emissions: Implementation and Validation

Jonathan F. Dooley<sup>1</sup>, Kenneth Minschwaner<sup>1</sup>, Manvendra K. Dubey<sup>2</sup>, Sahar H. El Abbadi<sup>3,a</sup>, Evan D. Sherwin<sup>3,a</sup>, Aaron G. Meyer<sup>2,b</sup>, Emily Follansbee<sup>2</sup>, and James E. Lee<sup>2</sup>

<sup>1</sup>Department of Physics, New Mexico Institute of Mining and Technology, Socorro NM 87801, USA

<sup>2</sup>Earth and Environmental Sciences, Los Alamos National Laboratory, Los Alamos NM 87545, USA

<sup>3</sup>Department of Energy Science & Engineering, Stanford University, Stanford CA 94305, USA

<sup>a</sup>Present Affiliation: Lawrence Berkeley National Laboratory, Berkeley CA 94720, USA

<sup>b</sup>Present Affiliation: The University of Utah, Salt Lake City, UT 84112

**Correspondence:** Jonathan F. Dooley (jonathan.dooley@student.nmt.edu)

**Abstract.** Methane (CH<sub>4</sub>) is a powerful greenhouse gas ~~with a global warming potential 84 times higher than carbon dioxide~~ ~~( $\rho$ ) over 20 years. is produced from many that is produced by a diverse set of~~ natural and anthropogenic ~~sources which can be further classified as biogenic or thermogenic in origin. The largest biogenic sources result from anaerobic decay such as~~ emission sources. Biogenic methane sources generally involve anaerobic decay processes such as those occurring in wet-  
5 lands, melting permafrost, or the ~~breakdown-digestion~~ of organic matter in the guts of ruminant animals. Thermogenic CH<sub>4</sub> ~~is generated during~~ sources originate from the breakdown of organic ~~matter-material~~ at high temperatures and pressure within the Earth's crust, a process which also produces more complex trace hydrocarbons such as ethane (C<sub>2</sub>H<sub>6</sub>) ~~and propane ( $\rho$ ).~~ ~~Emissions of thermogenic are dominated by the fossil fuel energy sector, and the presence of elevated along with can be used to distinguish oil and gas emissions from biogenic sources. This work outlines the.~~ Here, we present the development and deployment of an  
10 ~~Unmanned-Uncrewed~~ Aerial System (UAS) ~~outfitted with that employs~~ a fast (1 Hz) and sensitive (1 – 0.5 ppb s<sup>-1</sup>) CH<sub>4</sub> & C<sub>2</sub>H<sub>6</sub> sensor and ultrasonic anemometer. The ~~UAV-UAS~~ platform is a vertical-takeoff, hexarotor ~~vehicle-drone (DJI Matrice 600 Pro, M600P)~~ capable of vertical profiling to 120 m altitude and plume sampling across scales up to 1 km. ~~This system has been used for direct quantification of point sources, as well as distributed emitters such as landfills, with source rates as low as and up to.~~ Simultaneous measurements of CH<sub>4</sub> and C<sub>2</sub>H<sub>6</sub> ~~mixing-ratios~~ concentrations, vector winds, and positional  
15 data allows for source classification (biogenic versus thermogenic), differentiation, and emission rates without the need for modeling or a priori assumptions about winds, vertical mixing, or other environmental conditions. The ~~UAS has been deployed throughout the Southwest United States for system validation and targeted quantification of various sources emitting at or below the detection limits of other aircraft and satellite systems. This system~~ system has been used for direct quantification of methane point sources, such as orphan wells, and distributed emitters such as landfills and wastewater treatment facilities.  
20 With detectable source rates as low as 0.04 kg h<sup>-1</sup> and up to ~1500 kg h<sup>-1</sup>, this UAS offers a direct ~~and~~ repeatable method of horizontal and vertical profiling of emission plumes at scales that ~~provide complementary information for~~ are complementary to regional aerial surveys ~~as well as local and localized~~ ground-based monitoring.

# 1 Introduction

Methane (CH<sub>4</sub>) is the second-largest contributor to anthropogenic radiative forcing ~~and has a significantly higher, with a~~ Global Warming Potential (GWP) ~~than GWP-20~~ greater than 80× that of carbon dioxide (CO<sub>2</sub>) (Solomon et al. (2007); Schneising et al. (2020); Holmes et al. (2013)). ~~While the increased use of natural gas (primarily composed of~~ Methane is produced from many natural and anthropogenic sources which can be further classified as biogenic or thermogenic in origin. ~~The largest biogenic sources result from anaerobic decay such as wetlands, melting permafrost, or the breakdown of organic matter in the guts of ruminant animals. Thermogenic CH<sub>4</sub> after processing) for energy generation has helped to reduce emissions, supply chain leakage can reduce the environmental benefits of natural gas (Solomon et al. (2007); Karion et al. (2015); Johnson et al. (2019)). In addition to thermogenic sources from,~~ ‘natural gas’, is generated during the breakdown of organic matter at high temperatures and pressure within the Earth’s crust. The later process also produces more complex trace hydrocarbons such as ethane and propane collectively known as Natural Gas Liquids (NGLs). Coal mining, natural seeps, Oil and Natural Gas (O&NG) activities, ~~coal mining, and natural seeps, there are significant biogenic methane emissions from wetlands, biomass storage, and ruminant animals (Solomon et al. (2007); Cheewaphongphan et al. (2019)). Detection of ethane — and supply chain leakage each produce varying amounts of NGLs. While sometimes other gases predominate, e.g. CO<sub>2</sub>, all thermogenic sources contain some fraction ethane (C<sub>2</sub>H<sub>6</sub>, the second-largest component) (Kutcherov and Krayushkin (2010); Glasby (2006); Etiope and Sherwood-Lollar (2013)), and it is the second-most prevalent NGL in natural gas (Kutcherov and Krayushkin (2010); Hodnebrog et al. (2018); Solomon et al. (2007)). — is critical~~ processed for energy generation (Hodnebrog et al. (2018); Solomon et al. (2007); Simpson et al. (2012); Peischl et al. (2018)). Biogenic methane emissions do not contain ethane (Masson-Delmotte et al. (2023); Cheewaphongphan et al. (2019)) so that C<sub>2</sub>H<sub>6</sub> is therefore a critical marker for source attribution, particularly when distinguishing between biogenic and thermogenic methane emissions. ~~Kutcherov and Krayushkin (2010), Glasby (2006) and Etiope and Sherwood-Lollar (2013) have shown that thermogenic sources all contain some fraction ethane with methane, whereas biogenic sources contain only methane. (Solomon et al. (2007); Karion et al. (2015); Johnson et al. (2019)).~~ Accurately quantifying contributions from various sources, both spatially and temporally, is an important step towards building local, regional, and global CH<sub>4</sub> emission estimates as well as informing policy decisions.

The accuracy of regional and global methane emission estimates is limited due to the sheer number of unknown variables. There are two primary methods to estimate methane emissions: statistical analysis of source activity inventories, known as ‘Bottom-Up’ (BU) estimations, and ‘Top-Down’ (TD) estimates ~~which are~~ based on observations ~~constraining the atmospheric burden, often by satellites, from instruments deployed on satellite, aircraft, and/or ground-based observation networks (Heath et al. (2015); Schneising et al. (2020); Vaughn et al. (2018); Cheewaphongphan et al. (2019); Frankenberg et al. (2016)).~~ While these platforms (Heath et al. (2015); Schneising et al. (2020); Vaughn et al. (2018); Cheewaphongphan et al. (2019); Frankenberg et al. (2016)). A variety of BU and TD methods have been used to detect methane leaks (Frankenberg et al. (2016)) and have played an important role in environmental regulation and policy (Frankenberg et al. (2005)) and inform policy decisions (Heath et al. (2015)), ~~the two methods show persistent discrepancies (Vaughn et al. (2018); Peischl et al. (2018); Cheewaphongphan et al. (2019)).~~ Many BU ~~but~~ persistent discrepancies remain between the BU and TD methodologies (Masson-Delmotte et al. (2023); Solomon et al. (2007)). In general, BU and TD estimation methods ~~typically represent only~~ represent a snapshot in time and do not effectively

account for temporal variations ~~such as diurnal and seasonal variability. Multiple~~ due to diurnal, seasonal, and activity cycles. Recent studies have shown that O&NG methane emissions vary significantly in time (Lavoie et al. (2017); Johnson et al. (2019); Vaughn et al. (2018)) ~~indicating that~~ Lavoie et al. (2015); Johnson et al. (2019); Vaughn et al. (2018)) showing that more frequent and repeated measurements ~~may help to reduce and constrain uncertainties in emissions monitoring~~ (Schneising et al. (2020); Space Studies Board et al. (2019)) are important in helping to reduce uncertainties in emission monitoring (Frankenberg et al. (2005); Space Studies Board et al. (2019)).

Spaced-based systems such as the offer robust methods of monitoring CH<sub>4</sub> and other Greenhouse Gases (GHGs) at regional and global scales (Sherwin et al. (2023); Schneising et al. (2020)). However, most large-area satellites (Sentinel, Landsat) drop off in detection at ~1,000 kg h<sup>-1</sup> with only the very sophisticated or targeted systems able to quantify sources < 500 kg h<sup>-1</sup> (Sherwin et al. (2023)). These instruments for TD emission estimates are ideally supplemented with contemporaneous ground-based measurements to constrain the monitoring capabilities – e.g., Total Carbon Column Observing Network, TCCON (Vaughn et al. (2018); Péron et al. (2019)).

A common method for estimating GHG emissions ~~using aircraft~~ is a mass balance approach (Hiller et al. (2014); Karion et al. (2015, 2016)), which uses GHG concentration measurements upwind and downwind of target sources to isolate ~~source methane enhancements~~ the source from background concentrations (Chen et al. (2016); Frankenberg et al. (2016); Schwietzke et al. (2017); Johnson et al. (2019)). These measurements can be collected from aircraft ~~transecting the source plume~~ instruments along upwind and downwind transects (Frankenberg et al. (2016); Schwietzke et al. (2017)) or by simultaneous measurements using similar ground-based instruments installed upwind & and downwind of the sources (Chen et al. (2016); Gisi et al. (2012); Gisi et al. (2012); Saad et al. (2014); Heerah et al. (2021)). The accuracy of the latter method depends on ~~a~~ a relatively constant wind speed and direction during data collection. Therefore, ~~it is imperative to have~~ accurate knowledge of the target area's principal wind conditions ~~to properly install the instrument is required for proper instrument installation~~, and only those data obtained under favorable ~~meteorological~~ conditions can be used to accurately estimate the flux (Chen et al. (2016)). ~~Detailed modeling of meteorology over large domains (e.g., WRF) of data from multiple solar spectrometers has also been used to infer emissions but is uncertain when flows are complex~~ (Viatte et al. (2017); Heerah et al. (2021)). ~~Ground-based differential measurements can be useful for characterizing sources with higher spatial resolution than typical space-based instruments such as TROPOMI's horizontal resolution~~ (Schneising et al. (2020)). However, the required site analysis and the cost to deploy and maintain multiple ground-based sensors limit the number of surveys that can be conducted, especially in secluded, rural areas.

While satellites can monitor at a global scale, most remote sensing instruments must estimate wind speed and direction as well as the Boundary Layer (BL) height in order to calculate the source emission rate (Alexe et al. (2015); Frankenberg et al. (2005); Parker et al. (2019)). The estimated detection thresholds for satellite instruments is in the range of 100–10,000 kg h<sup>-1</sup> (Gisi et al. (2012); Lavoie et al. (2017)). Aircraft quantification methods generally drop off around 10 kg h<sup>-1</sup> (Jacob et al. (2022)), and recent work by Sherwin et al. (2023) ~~indicates a lower detection limit of between 500 kg h<sup>-1</sup> for the highly sensitive instruments so that it is difficult or impossible to quantify low-emitting sources using combined ground, aircraft, and 1000 for most satellite systems. Similar to satellites, aircraft detection systems require a priori wind information around the source location. However, some aircraft systems are~~

able to infer the BL height and have a minimum detection thresholds of  $2\text{--}10\text{ kg h}^{-1}$  due to proximity and higher spatial resolution (Duren et al. (2019)). Combined measurements using both aircraft and complementary satellite data result in more robust TD emission estimates, but scheduling and implementing contemporaneous measurement from both air and space can be prohibitively difficult and time-consuming. satellite data to constrain and validate the estimates. Ground-based detection systems are the most straightforward and accessible methods, but effective site monitoring is highly dependent on wind directions. Column-averaged measurement techniques using Fourier Transform Spectrometers (FTS) also require BL height estimations and are unable to provide vertical profiles of source plumes.

There is a need for direct, repeatable, and cost-effective methods for detecting and quantifying  $\text{CH}_4$  emissions from relatively small sources ( $< 1\text{ kg h}^{-1}$ ), which do not require a priori assumptions.

~~This paper details the integration, testing,~~ Small Uncrewed Aerial Vehicles (UAVs) offer new approaches to airborne air pollution and emission monitoring over scales and locations which are difficult to detect or access with other regional monitoring systems (Villa et al. (2016); Burgués and Marco (2020)). While designs can vary dramatically between models, UAVs are either fixed or rotary-wing platforms. Fixed-wing UAV are typically able to cover larger areas and generally allow more options for sensor mounting configurations, but they are unable to hover and quickly adapt to environmental conditions while tracking emission plumes. Rotary wing platforms – also known as Vertical Takeoff And Landing (VTOL) or Multirotor UAVs – generally have lower required operating velocities and have the ability to hover and can therefore be used for more complex, discontinuous missions at higher spatial resolution (McKinney et al. (2019); Villa et al. (2016); Burgués and Marco (2020)). Multi-rotor UAV usually have between 4 and ~~initial results of a new methane flux measurement system. It utilizes a compact mid-IR spectrum analyzer and lightweight anemometer onto a commercially available Unmanned Aerial Vehicle (UAV) for efficient, repeatable flux measurement and characterization of anthropogenic sources. This novel~~ 8 individual propellers which to generate thrust and the power consumption results in shorter flight times than their fixed-wing counterparts, but they do not require specialized equipment or runways for takeoff/landing and recent advances in control technology have made multirotor systems easier to reliably operate.

A major issue with fixed-wing systems is that the higher operating velocities and minimum height requirements result in low detection probabilities during site surveys (Barchyn et al. (2019)). Rotary UAV systems do not require a minimum velocity to stay aloft, and can therefore be outfitted with a wider range of equipment for physical and chemical sensing (Hollenbeck et al. (2018); Shah et al. (2019); McKinney et al. (2019); Villa et al. (2016); Burgués and Marco (2020)). For instance, onboard anemometers for in situ wind speed/direction have been shown to be more accurate onboard VTOL platforms while higher relative winds and aerodynamic flows around fixed-wing platforms often result in less accurate in situ measurements (Hollenbeck et al. (2018)). While multirotor UAV have a significant propeller wash effect below the body, induced winds are negligible when anemometers are mounted above the shallow inflow layer (Barbieri et al. (2019); Hollenbeck et al. (2018); Villa et al. (2016)).

The fast development of commercial UAV and low-weight sensors has driven a multitude of scientific studies which would have been difficult or impossible to conduct over a decade ago. Both inverse modeling and mass-balance approaches have been used to calculate total emissions across a wide range of spatial scales. McKinney et al. (2019) deployed a hexarotor UAV

130 outfitted with adsorbent cartridges to collect biogenic Volatile Organic Compound (VOCs) emissions at various locations in central Amazonia. Shah et al. (2019) calculated 3-D flux densities by fitting direct measurements of a downwind CH<sub>4</sub> plumes to near-field Gaussian plume models. Olaguer et al. (2022) used contemporaneous UAV and mobile ground-based measurements to estimate biogenic CH<sub>4</sub> emissions from a landfill. Bel Hadj Ali et al. (2020) compared multiple ground-based emission monitoring techniques with downwind plume measurement fitted to Gaussian plume models. Gálfalk et al. (2021) piloted a small quadcopter to fully surround a known biogenic methane hotspot for mass balance emission estimates < 200 kg h<sup>-1</sup>.

135 This study describes the development and implementation of a new Uncrewed Aerial System (UAS) to address critical areas of research by (a) accurately and directly quantifying emissions on small spatial and temporal scales, especially in hard to reach places; (b) constraining BU inventories driven by small-scale estimations; and (c) separating and attributing thermogenic and biogenic sources. The New Mexico Tech (NMT) UAS design combines rapid sampling of chemical and meteorological data with a mobile platform capable of vertical and horizontal profiling relative to target sources, for ~~high-resolution-spatial-direct~~ and high resolution sampling of emission plumes. A commercially available UAV is outfitted with a multi-sensor onboard payload including a compact mid-IR spectrum analyzer and lightweight anemometer for efficient, repeatable quantification  
140 and characterization of various localized anthropogenic sources.

## 2 ~~System Design~~Methods

### ~~The full Unmanned-~~

#### 2.1 System Design

145 The full Uncrewed Aerial System (UAS) is depicted in figure 1. It includes four main components: (1) mobile Mid-IR methane and ethane sensor (Aeris MIRA Pico) (2) lightweight 3D vector wind and environmental sensor (Anemoment Trisonica Mini) (3) ~~Unmanned Uncrewed~~ Aerial Vehicle (~~UAV~~, DJI Matrice 600 Pro, M600P) (4) onboard computer for system monitoring and data collection.

#### 2.2 ~~Onboard Sensors~~

##### 2.1.1 ~~Methane and Ethane Sensor~~

150 The MIRA (Mid-InfraRed Analyzer) Pico Leak Detection System (LDS) developed by Aeris Technologies employs a solid state laser and multi-pass absorption cell with a spectral band pass between 2.5 and 4.7  $\mu\text{m}$ . The wide spectral range allows for simultaneous ~~mixing-ratio~~ measurements of both CH<sub>4</sub> and C<sub>2</sub>H<sub>6</sub> mixing ratios with a precision of 1 ppb s<sup>-1</sup> and 0.5 ppb s<sup>-1</sup>, respectively (Aeris Technologies Inc (2019); Scherer (2017)). ~~The response time is a function of the gas flow rate through the cell, which can be adjusted via the speed of a small gas pump; flow rates for our system correspond to a response time of .5~~ The  
155 MIRA Pico is outfitted with a flexible length of tubing (see section 2.1.1) and the constant pump flow rate results in a phase lag of ~2 s based on laboratory tests of the decay in pulsed gas releases. The MIRA has been used extensively on the ground

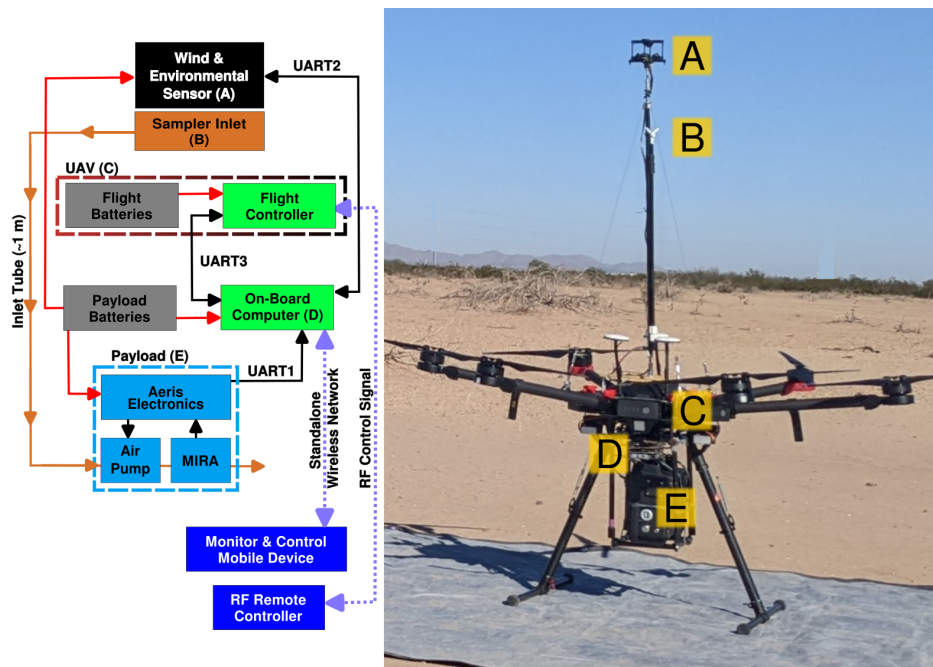


**Figure 1.** Uncrewed Aerial System (UAS) design overview. (Left) System block diagram: (A) Trisonica Mini Weather Sensor (TWS), (B) Gas sampler inlet, (C) Matrice 600 Pro Uncrewed Aerial Vehicle (M600P), (D) Raspberry Pi 4 on-board computer, and (E) Aeris MIRA Pico methane and ethane sensor. (Right) Flight-Ready UAS collecting ground data prior to takeoff. TWS and sampler inlet (A and B) mounted on a carbon fiber tube mast above the M600P’s propeller inflow layer (‘rotor wash’).

including controlled release tests at Colorado State University’s (CSU) METEC facility to find and quantify leaks (Travis et al. (2020)).

### 2.1.2 Onboard Anemometer and Weather Sensor

160 In addition to gas-mixing-ratioshydrocarbon concentrations, direct flux quantification requires measurements of vector winds, temperature, and pressure. The system includes an ultra-light, 3D sonic anemometer: the Trisonica Mini Weather Sensor (TWS) by Anemoment has a mass of 50 g with a volume of less than 450 cm<sup>3</sup> (Anemoment LLC (2022, 2018)). ~~Direct, in situ measurements of vector winds during flight removes the need to assume consistency in speed & direction as the UAS rapidly changes location and altitude throughout each flight.~~ Additionally, environmental measurements can also be used  
 165 as a way to detect and adapt to unsafe conditions during flights (Hollenbeck et al. (2018)). The TWS senses vector winds ( $|\mathbf{u}|$ ), temperature ( $T$ ), and pressure ( $P$ ) at 5 Hz with an accuracy of  $\delta|\mathbf{u}| = 0.35 \text{ m s}^{-1}$ ,  $\delta u_m = \delta v_m = 0.2 \text{ m s}^{-1}$ ,  $\delta T = 2 \text{ C}$ , and  $\delta P = 10 \text{ hPa}$ , respectively (see table 1).

### 2.1.3 Unmanned Uncrewed Aerial Vehicle (UAV)

The UAV (DJI Matrice 600 Pro, (M600P)) is a hexarotor vertical takeoff and landing aircraft that is capable of flying with relatively large payload masses of up to 5.5 kg. This powerful and mobile platform became commercially available in 2014 and has been used in a variety of scientific and commercial applications (McKinney et al. (2019); Villa et al. (2016); Hollenbeck et al. (2018)). The M600P can be remotely piloted up to a distance of up to 5 km at a maximum altitude of 125 m above ground level. Flight times depend on factors such as payload mass, winds, and flight pattern. Under typical winds of 2–4 m s<sup>-1</sup> and the standard total payload mass of ~3 kg, total flight times range between 18 and 25 min. We employ dual battery packs that are cycled between flying and charging in the field, ~~allowing for~~; due to battery life and charging limitations, the UAS typically can accommodate about one flight per hour. Additionally, the flux quantification method described in section 2.2 relies on relatively stable wind fields around the source, optimally between 2 and 6 m s<sup>-1</sup>.

The M600P is controlled via proprietary software & firmware with an expansive API for telemetry logging and flight control (Aeris Technologies Inc (2019)). However, the reliance on proprietary software limits system customizability and sensor integration (see section ~~???~~2.1.2). While it is possible to automate flight plans for the M600P, it is more important for the operator to maintain control of the UAS throughout the entire flight to account for changing or unexpected flight conditions.

## 2.2 Sensor Integration

~~Each of the three main devices (MIRA Pico, TWS, and M600P) has its own output data stream that must be separately parsed and then temporally synchronized with the other streams. The M600P does not support the use of DJI's proprietary 'Payload SDK'—firmware enabling sensor data to be transmitted along with the RF control signal. Therefore, remote monitor and control of the fully-integrated UAS is handled independently of the M600P via an onboard device for both acquisition and transmission. A 4<sup>th</sup> generation Raspberry Pi (RPI) single board computer is the ideal choice due to its size, weight, and programmability via the Linux Kernel. The RPI is powered independently via a payload battery (see figure 1) allowing for ground-based data collection between flights, typically while the UAV batteries are charging.~~

### 2.1.1 Payload Sensor Mounting

The both the RPi onboard computer and MIRA Pico mount to the M600P underside as shown in figure 1. The UAV-M600P achieves flight by funneling air downwards to create thrust, constantly displacing air around the vehicle's body in the process (Dà Jiāng Innovations (2018)). Computational fluid dynamics simulations carried out by McKinney et al. (2019) determined that the Matrice 600 Pro causes disturbances up to 5 m below the UAV-M600P's center of mass; however, the magnitude of the disturbances drops off quickly at a height of 60 cm above the UAV-M600P body.

The TWS mounts to a mast made of lightweight, carbon fiber tubing (0.5 in diameter) anchored near the UAV-M600P's center of mass. This places the TWS ~85 cm above the UAV-M600P and above the shallow inflow layer generated by propellers during normal flight. At this height above the propellers, air disturbances are below the noise floor of the TWS (~~~0.1 m s<sup>-1</sup>~~~0.2 m s<sup>-1</sup>) or easily calibrated out during data processing. A ~1 m section of flexible tubing connects the pay-

200 load's gas cell to a ~~dual-opening~~ sampling port approximately 80 cm above the body of the M600P. This ~~tubing-physical offset between the MIRA and sampling port~~ introduces a phase lag of  $\sim 2$ s between the measured ~~concentration-time series-MIRA concentrations~~ and the TWS data, which is accounted for ~~in-prior to~~ the calculation of instantaneous fluxes. ~~The sampler port is outfitted with a plastic Y-shaped inlet for redundant openings to decrease the chance of damaging the pump due to debris clogging the inlet.~~

205 While the TWS has an integrated magnetometer to measure heading, this device is intended for stationary deployment in an open location where averaging of compass readings can result in a relatively accurate direction. However, any magnetic disturbance created from adjacent devices or operating motors perturb the heading measurements. In contrast, the M600P has a triple redundant positioning system with an accuracy of  $< 3^\circ$  at 200 Hz. The TWS must be physically aligned with the more accurate heading data from the M600P's Inertial Measurement Unit (IMU) to accurately calculate static-frame vector winds  
210 (more in Section 2.2).

In order to ensure proper alignment, the M600P is set up facing North with the TWS mounting point tightened so that the anemometer's North arm is facing the same direction. The MIRA Pico and Onboard Computer are both mounted under the body of the ~~UAV-M600P~~ as shown in figure 1. Initial ~~UAV-M600P~~ test flights revealed that payload mounting at this location improves flight performance, especially during takeoff and landing, due to the lower center of mass.

### 215 **2.1.2 ~~Onboard Data Logging and Transmission~~**

~~Each of the three main devices (MIRA Pico, TWS, and M600P) has its own output data stream that must be separately parsed and then temporally synchronized with the other streams. The M600P does not support the use of DJI's proprietary 'Payload SDK' — firmware enabling sensor data to be transmitted along with the RF control signal. Therefore, remote monitor and control of the fully-integrated UAS is handled independently of the M600P via an onboard device for both acquisition and transmission. A 4<sup>th</sup> generation Raspberry Pi (RPi) single board computer is the ideal choice due to its size, weight, and programmability via the Linux Kernel. The RPi is powered independently via a 10 Ah payload battery (see figure 1) allowing for ground-based data collection between flights, typically while the M600P batteries are charging.~~

220

## **2.2 Relative Wind Adjustments**

The Trisonica Mini Weather Station (TWS) is designed for static installation with one arm facing north (Anemoment LLC  
225 (2022)) and will therefore produce incorrect results when the device's heading ('yaw',  $\psi$ ) is not a multiple of  $2\pi$  (Anemoment LLC (2022, 2018); Hollenbeck et al. (2018)). In addition, the motion of the ~~UAV-M600P~~ during data collection induces an apparent wind that is folded into the TWS wind measurement. Transforming the raw TWS vector wind measurements ( $\mathbf{u}_m = [u_m, v_m, w_m]$ ) to Earth-fixed coordinates therefore requires accurate, real-time measurements of  ~~$\psi$  and UAV- $\phi$  and UAS~~ velocity ( $\mathbf{V}_s$ ).

230 In order to transform ~~raw TWS wind~~ the measured TWS data to static-frame ~~vector winds~~ coordinate system, we apply a standard Galilean transformation  ~~$\mathbf{u} = \mathbf{R}(\phi)\mathbf{u}_m + \mathbf{V}_s$~~  or as shown in equation 1.



$$\mathbf{u} = \mathbf{R}(\phi)\mathbf{u}_m + \mathbf{V}_s = \begin{bmatrix} \cos(\phi) & \sin(\phi) & 0 \\ -\sin(\phi) & \cos(\phi) & 0 \\ 0 & 0 & 1 \end{bmatrix} \begin{bmatrix} u_m \\ v_m \\ w_m \end{bmatrix} + \begin{bmatrix} V_x \\ V_y \\ V_z \end{bmatrix} = \begin{bmatrix} u \\ v \\ w \end{bmatrix} \quad (1)$$

Here,  $\mathbf{u}_m = [u_m, v_m, w_m]$  are the TWS-measured vector winds,  $\mathbf{u} = [u, v, w]$  is the corrected wind speed in Earth-fixed coordinates, and  $\mathbf{V}_s = [V_x, V_y, V_z]$  is the instantaneous UAS velocity.  $\mathbf{R}(\phi)$  is the counter-clockwise (CCW) Euler rotation matrix about the vertical axis ( $\hat{z}$ ) where  $\phi$  is the heading (yaw) of the M600P.

Rotations around the  $\hat{y}$  and  $\hat{x}$  axis — caused by variations in UAV-M600P pitch ( $\theta$ ) and roll ( $\varphi$ ), respectively — are ~~neglected since changes in  $\theta$  and  $\varphi$  are negligible~~ both generally less than  $3^\circ$  during steady, level flights ~~through the source plume and are therefore neglected in equation 1. The instantaneous pitch and roll can be greater than  $15^\circ$  when the M600P is being maneuvered to different altitudes between transects, but measurements collected during these spurious adjustments are filtered out during the flux quantification process (see section 2.2).~~

A time series of the TWS-measured raw winds during a typical flight is shown in figure 2, along with the derived static-frame vector winds based on the M600P headings and velocities throughout the flight. The raw wind measurements show clear signatures of back-and-forth, quasi-horizontal motions of the M600P during sampling of a methane plume. Winds adjusted for changes in heading and horizontal translation show a more realistic, continuous structure, but some residual effects can be discerned at turning points in the flight, when the platform's horizontal acceleration is large and the corresponding pitch and roll angles become appreciable. In general, pitch and roll angles during level, steady flight sections are less than  $3^\circ$  (see figure A1), but these angles can increase to  $10^\circ$  or more during rapid horizontal accelerations. We estimate that a  $15^\circ$  pitch or roll angle may introduce an error of up to 4% in measured horizontal winds, therefore data obtained during turning points and/or deliberate changes in flight altitude are screened from the analysis of methane fluxes (see section 2.2). The adjusted and filtered winds have been compared to tower anemometer measurements during controlled release validation experiments (section 3) and these show agreement to within  $\pm 15\%$  over  $\sim 1$  minute averages and with spatial separations of about 100 m. Individual wind components have also been compared in the field (see figure A2), when the UAS was flown between 10 and 30 m downwind of a static, single-component wind gauge. Comparison of 5-second averages show agreement to within 10% over a range of winds between 2 and  $7 \text{ m s}^{-1}$ .

### 2.3 Background ~~Mixing-Ratio-Concentration~~ Estimation

While the MIRA Pico is highly sensitive with a large dynamic range ( $\sim 20 \text{ ppb} < \chi_{\text{CH}_4} < 4000 \text{ ppm}$ ) (~~Aeris Technologies Inc (2019); Meyer et al. (2022); Follansbee et al. (2024)~~), there are observable levels of semi-periodic drift in the measured ~~mixing-ratios-mole fractions~~ for both hydrocarbons at the ppb level. This effect is especially noticeable for  $\chi_{\text{C}_2\text{H}_6}$ , partly because ambient ~~mixing-ratios-for-C<sub>2</sub>H<sub>6</sub> concentrations~~ are generally  $\sim 100\times$  smaller than  $\text{CH}_4$ . In addition to these instrumental drifts, the raw concentration measurements ( $\chi$ ) may reflect actual changes in ~~background-mixing-ratios-ambient background~~. Nearby point sources do not directly influence these background variations; instead they may be related to regional-scale emissions and meteorological influences such as winds and stability at the mesoscale level. Both of

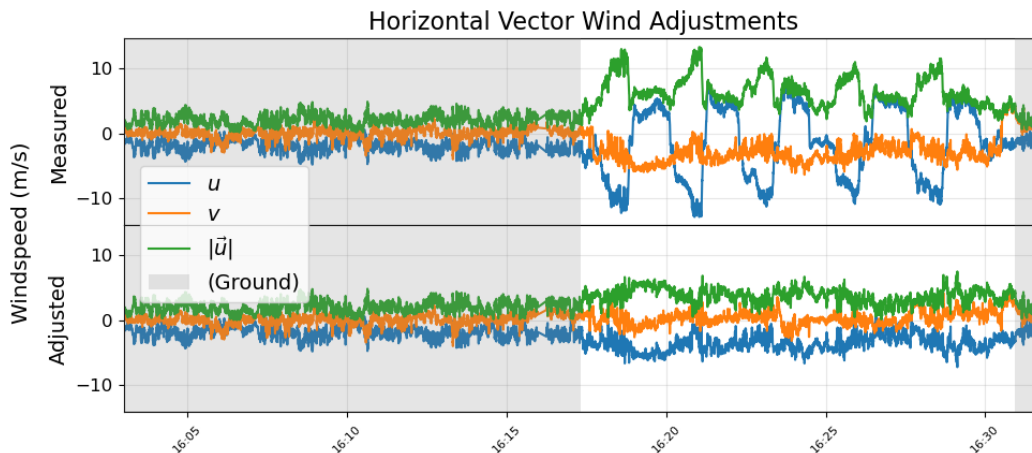


**Figure 2.** Raw measured vector winds: (top) and heading/velocity corrected vector winds (bottom) before, during, and after flight. Pre- and post-flight ground wind speeds at the takeoff location highlighted in gray.

these effects contribute to structure in the measured background ( $\chi_0$ ), which must be accurately quantified in order to isolate enhancements from the target source. This background variability generally occurs over periods of minutes and is independent  
 265 between  $\chi_{\text{CH}_4}$  and  $\chi_{\text{C}_2\text{H}_6}$ , so that direct comparison prior to baseline-background removal can be misleading, especially over longer period datasets.

The UAS measurement strategy involves repeated cross-wind sampling of the transects through the dispersing plume downwind of a target source (as discussed in more detail in section ??2.1). The resulting time series of mixing-ratio-concentration data contains a number of finite-width enhancements superimposed on a slowly varying background, as shown in figure 3-A.  
 270 Over the course of these measurements, the solar insolation was increasing and the wind speed and direction were changing, which led to a monotonic increase in the background methane concentration as seen with the increasing background. It should be noted that each plume "spike" in figure 3A should not be expected to have the same peak height or width, since these plume intersects all occur at different times, altitudes, and downwind distances.

The background,  $\chi_0$ , is estimated by fitting a polynomial to the measurements outside the plume. After extensive testing, the  
 275 procedure described below and outlined in figure 3 proved to be the most effective method of filtering inter-plume samples.

The raw  $\chi$  timeseries is initially 3-point-smoothed ( $\tilde{\chi}$ ) to decrease the effect of noise in the identification of the plume edges before further filtering (figure 3A). The gradient of  $\tilde{\chi}$  is then used to detect abrupt changes to  $\tilde{\chi}$  which are indicative of the UAS entering or exiting the higher-concentration plume, as shown in -3. Samples where  $\nabla\tilde{\chi}$  is greater than a specified threshold (get filtered out (i.e., more than  $\pm\gamma\sigma$ , where  $\gamma$ ) are determined to be 'in-plume'. For this analysis, we determined  
 280 a threshold of  $0.2 * \sigma$  reliably distinguished between in-plume and 'background' periods is a predefined constant,  $\pm 0.2\sigma$  in figure 3B and in the subsequent analysis of measurements presented here). This gradient filter removes the majority of the inter-plume samples, leaving behind the 'background' samples which vary at a much lower frequency. The gradient filter

output is then thresholded to remove any remaining. However, the gradient filter is imperfect and occasionally some inter-plume measurements; the final output samples are from outside the samples are not removed during this step. Therefore, a followup outlier filter is used to remove samples which are significantly far from the mean of the samples (more than one standard deviation from the mean in figure 3C). The remaining samples are taken to be the background with respect to the target plume (background measurements,  $\tilde{\chi}_{bg}$ ) and a variable order polynomial (deg(3) in figure 3) is fit to these samples. The regression coefficients that best fit. The polynomial order is empirically selected based on the individual dataset, usually between second and fourth order (cubic in figure 3D). Higher order polynomials have can affect the edges of the fitted timeseries but generally, higher order polynomials ( $> 4$ ) are not required after appropriately setting the gradient and outlier filter threshold parameters. The polynomial regression coefficients fitting  $\tilde{\chi}_{bg}$  are then applied to the original  $\chi$  sampled timestamps to estimate  $\chi_0$  for each independent hydrocarbon and dataset. This estimated background is then subtracted from the original timeseries to get the isolated source plume enhancements,  $(\chi - \chi_0)$ , for both  $\text{CH}_4$  and  $\text{C}_2\text{H}_6$ .

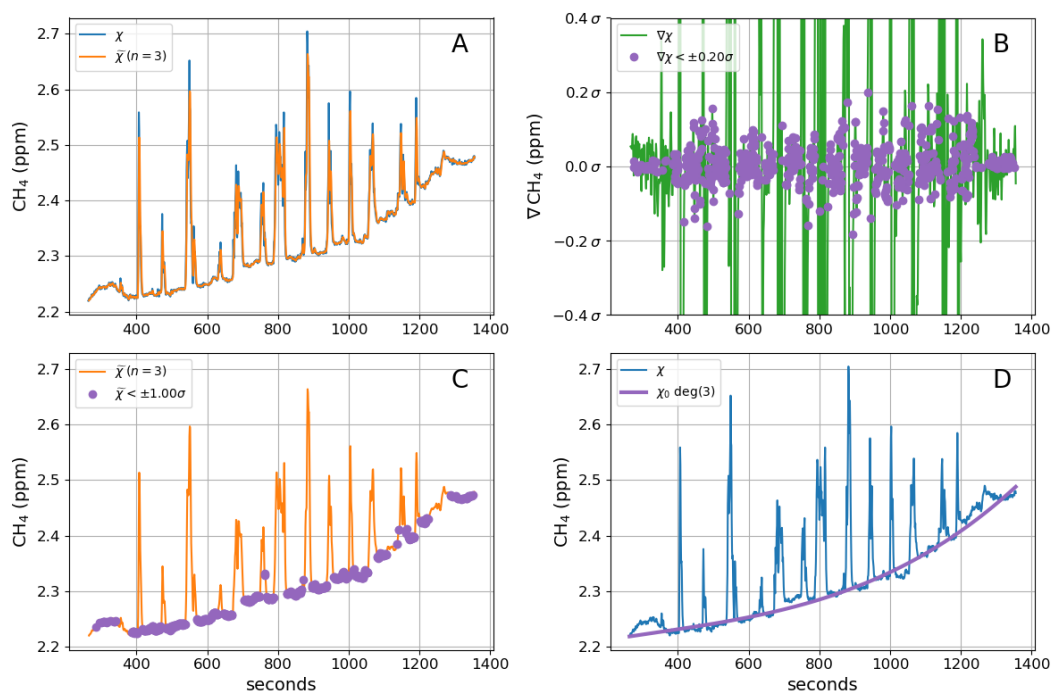


**Figure 3.** Time series of methane measurements during a typical flight, illustrating the procedure for background estimation and removal. The flight involved multiple cross-sections through the downwind plume of a known point emitter, and the plume enhancements in methane are visible as large spikes in the methane time series. (A) 3-point smooth raw data. (B) gradient filter to detect the majority of in-plume samples. (C) split remaining samples into segments and remove statistical outliers from each segment. (D) 3rd order polynomial fit using remaining samples; resultant regression coefficients used with initial (non-smoothed) raw data samples used to estimate background. Estimated CH<sub>4</sub> emission rate for this dataset is  $0.378 \pm 0.147 \text{ kg h}^{-1}$  (see section 2.2).

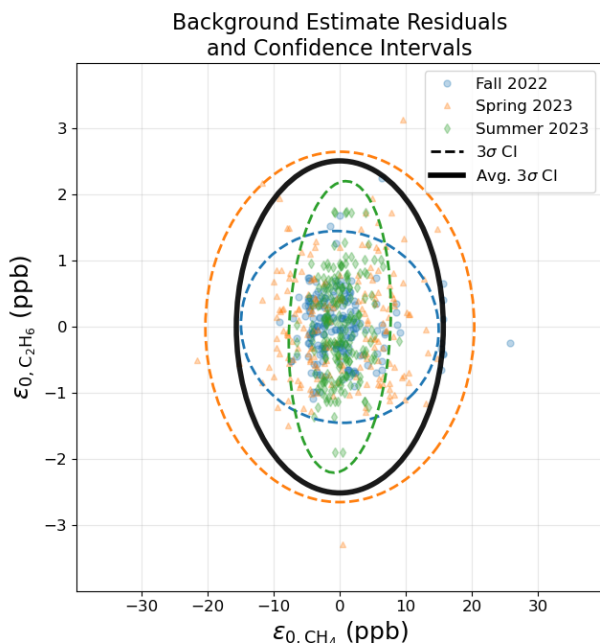


**Figure 4.** Residuals from the  $\text{CH}_4$  and  $\text{C}_2\text{H}_6$  background polynomial fit (outlined in figure 3) for three independent flights. The  $3\sigma$  confidence interval (99.7%) for each dataset is shown with a dashed line, highlighting the variability in the background estimates due to different sources and environmental conditions. The average  $3\sigma$  confidence interval, calculated from 28 flights during 2022 and 2023, is overlaid with a solid ellipse.

Figure 4 presents the distribution of  $\text{CH}_4$  and  $\text{C}_2\text{H}_6$  background estimate residuals ( $\varepsilon_0 = \chi_0 - \tilde{\chi}_{bg}$ ) from three independent flights around different source types. These three datasets were specifically chosen to highlight the variability in  $\varepsilon_0$  caused in part by the source strength and environmental conditions. The average  $3\sigma$  confidence interval (99.7%) calculated from more than two dozen flights is approximately 16 ppb for  $\text{CH}_4$  and 2.5 ppb for  $\text{C}_2\text{H}_6$ . This minimum detection limit governs the lower bounds on source strengths and fluxes that can be quantified with this UAS (further discussed in section 2.3)

## 2.4 Plume Simulations

Idealized Gaussian plume models are a reasonable first approximation for an emission plume. This section describes the modeling analysis that was conducted to develop optimal flight patterns and sampling strategies for the UAS. In these idealized simulations, emissions from the target source are held constant and surrounding environmental winds are steady during the M600P's 15 to 25 min flight time. Gaussian models offer a reasonable approximation for the structure and evolution downwind of the source's emission plume under these conditions (Shah et al. (2019); Stockie (2011); Jacob et al. (2022); Seinfeld and Pandis (2006); ), but it should be emphasized that source fluxes reported in this work do not rely on the results of Gaussian plume simulations

or inverse modelling (e.g., Jacob et al. (2022); Shah et al. (2019); Stoeckie (2011); Meyer et al. (2022); Follansbee et al. (2024) )-see section 2.2).

The Gaussian plume equation for the mass density of a gas ( $C$ , units of  $\text{kg m}^{-3}$ ) downwind of a point source emitter is shown in equation 2.

$$310 \quad C(x, y, z) = \frac{Q}{|\mathbf{u}|} \cdot \frac{1}{2\pi\sigma_y(x)\sigma_z(x)} \cdot \exp\left[-y^2/(2\sigma_y(x)^2)\right] \cdot \exp\left[-(z-H)^2/(2\sigma_z(x)^2)\right] \quad (2)$$

$Q$  is emission rate ( $\text{kg s}^{-1}$ ),  $\mathbf{u}$  is the constant horizontal wind speed ( $\text{m s}^{-1}$ ),  $\sigma_z$  &  $\sigma_y$  are standard deviations for Gaussian distributions, in units of meters, which are generally derived using stability classes (Seinfeld and Pandis (2006); Seinfeld and Pandis (2006); ).  $H$  is the height of the source (m).  $C$  is the estimated increase in gas density at position  $x$  (directly downwind, centerline),  $y$  (horizontal from centerline), and  $z$  (vertical from centerline) given in meters. It is important to make the distinction between the mass density,  $C$  ( $\text{kg m}^{-3}$ ), and the volume mixing ratio mole fraction  $\chi$  ( $\text{mol mol}^{-1}$ ) measured by the MIRA Pico. The conversion between the two is  $C = \eta\rho\chi$  where  $\eta$  is the ratio of molar masses of the gas to that of air, and  $\rho$  is the air density ( $\text{kg m}^{-3}$ ).

Simulated Gaussian Plume ( $Q = 25.00 \text{ kg/hr}$ ,  $|\vec{u}| = 2.0 \text{ m/s}$ )

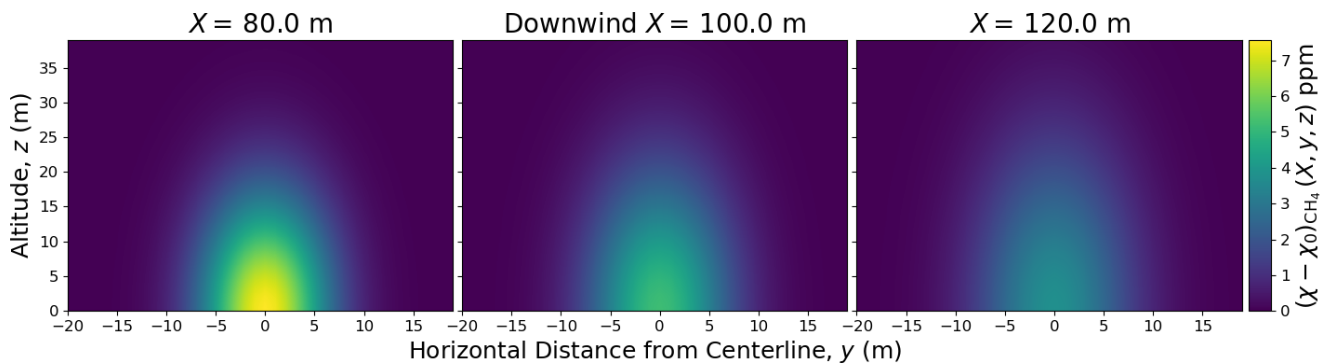


**Figure 5.** Cross-sections of modelled Gaussian plume under conditions of low wind (2 m/s) and high solar insolation (stability class "A" from Woodward (1998)). Each panel depicts the Gaussian plume cross-section at distance  $X$  downwind of the source. The horizontal distance,  $y$ , is with respect to plume centerline and the vertical distance  $z$  is above ground level. The plume model assumes a steady wind field and constant emission rate from the source.

Figure 5 shows cross-sections of a Gaussian plume simulated at three downwind distances from a  $25 \text{ kg h}^{-1}$  point source. Mean winds in this case are  $\sim 2 \text{ m s}^{-1}$  and the stability class corresponds to high solar insolation. As expected, the simulated plume becomes more dispersed, and broadens both horizontally and vertically with increasing distance from the source. Plume enhancements in methane range between 1 and 5 ppm, which are easily detectable with this system, and the horizontal and vertical scales ( $\sim 50 \text{ m}$ ,  $\sim 30 \text{ m}$ ) are readily accessible to the UAS.

### 3 Deployment

325 This section describes the preliminary flight preparation for the UAS based on the modelling and UAV flight time. If both emissions from the target source and surrounding environmental winds are relatively steady during the M600P's to flight time, then Gaussian models offer a reasonable approximation the expected structure that could be observed in methane enhancements downwind of the source (Seinfeld and Pandis (2006); Shah et al. (2019); Stockie (2011)). The Gaussian modeling discussed in the previous section helps to guide and describe the sampling strategy for target sources, but it should be emphasized that source fluxes reported in this work do not involve Gaussian inverse modelling from direct measurements (see section 2.2).

#### 330 2.1 Flight Pattern

The full UAS setup and pre-flight checks can be completed in under 15 min and any certified remote pilot, or person under the supervision of a certified pilot (Federal Aviation Administration (2021)), can operate and maneuver the UAS around target sources for direct plume sampling—a target source's emission plume. Part of the setup process involves the verification of MIRA measurements for both CH<sub>4</sub> and C<sub>2</sub>H<sub>6</sub>. Prior to each flight, a small canister of natural gas with a known composition (~7% C<sub>2</sub>H<sub>6</sub>:CH<sub>4</sub>) is rapidly opened and closed about 1 m upwind of the UAS gas inlet. This pre-flight release 'pulse' is measured on the MIRA to test for any lag or unexpected gain offset on either of the channels. As discussed in section 2.3, the raw concentration measurements can be biased due to a quasi-periodic sensor drift which must be estimated and removed before comparing the channels. This step is completed during data processing after each deployment, and it should be noted that the results from each of these controlled pulses has been consistent to within a fraction of the known C<sub>2</sub>H<sub>6</sub>:CH<sub>4</sub> ratio (<1% disagreement) across all deployments between 2021 and the present.

335

340

The flight time of ~20 min constrains the types of flight patterns that can be used to quantify source emission rates.

In order to maximize the number of in-plume samples within a relatively short flight period, our strategy is to remain downwind of the source and fly horizontal 'transects' perpendicular to the mean wind direction. This curtain or boustrophedonic flight is perpendicular to the average wind direction, and involves multiple cuts through the plume in order to measure both the in-plume concentrations,  $\chi$ , and the ambient or background concentrations used to determine  $\chi_0$ . Each individual transect through the downwind plume is at a relatively constant altitude and horizontal velocity between 2 and 5 m s<sup>-1</sup>, depending on the wind conditions and proximity to the source. Transects are typically 50 m to 1 km in length, depending on terrain, wind variability, and source distribution and downwind distance. Extended sources and measurements collected at larger downwind distances from the source require longer transects to ensure that the dispersing plume gets fully traversed during each transect.

345

350

The ability to quickly adjust altitude between each of the individual transects allows for direct measurements of the plume's vertical structure in addition to the horizontal dispersion.

Direct measurements of a source plume with the MIRA Pico sensor requires the UAS to be physically maneuvered downwind of the source. While a steady-state Gaussian plume model can be used for flux inversions (e.g., Jacob et al. (2022); Shah et al. (2019); Stockie (2011); Seinfeld and Pandis (2006); Woodward (1998); Bhattacharya (2013)), these models represent plume dispersion probabilities which are not generally observed in the superposition of horizontal transects through the plume.

355

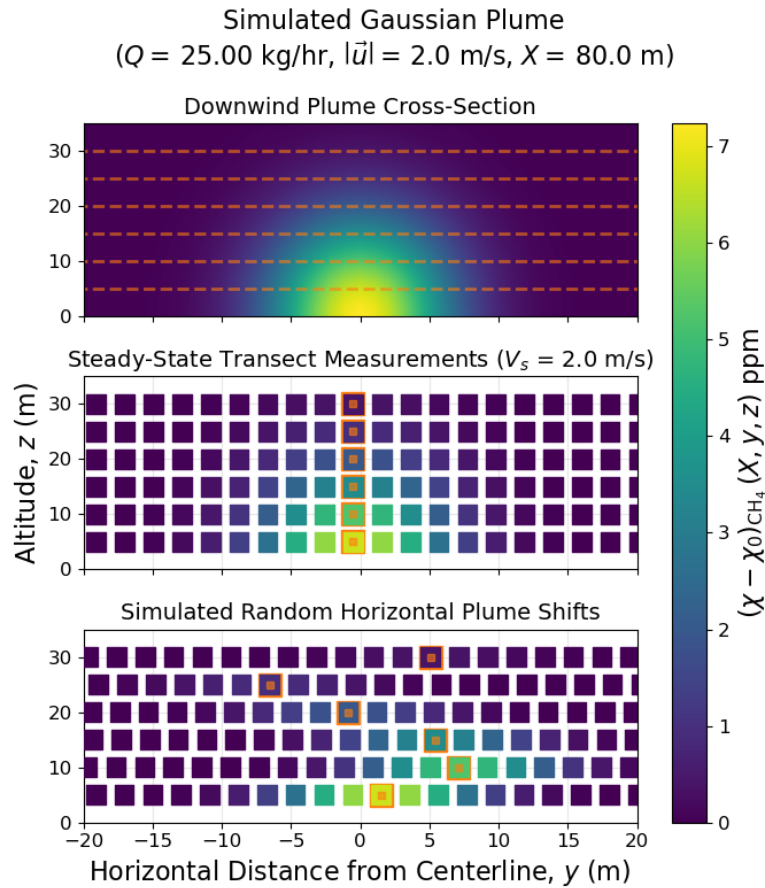


**Figure 6.** Simulated flight through Gaussian plume: (*top*) cross-section of plume  $X$  meters directly downwind of source, simulated transects shown as dotted lines. (*middle*) Resample of modelled cross-section at constant horizontal transect velocity  $V_s$ . (*bottom*) Random shifts in centerline horizontal position, simulating variable wind conditions and temporally separated plume transects.

During direct measurements, large-scale turbulence in the wind flow results in changes to the plume's size and relative location throughout the measurement period. Based on simple scaling arguments, we expect that plume variability is largest in the horizontal plane due primarily to wind directional variability. Figure 6 shows multiple simulated transects through a Gaussian plume's downwind cross-section in the case of a steady-state flow. We simulate the stochastic variability in the plume by introducing random shifts in centerline between each of the temporally separated transects, which can be seen at the bottom of Figure 6. This pattern is generally more consistent with our observations in comparison to the steady state model. However, the stochastic model shows that total plume flux is unaffected by horizontal plume displacements, provided that the integral is taken along horizontal transects.

## 2.2 Direct Flux Quantification

365 The data collected from a single flight is broken into  $K$  individual transects through the source's downwind plume, each transect representing data collected at a nearly-constant altitude,  $z$ , and non-zero horizontal velocity,  $\mathbf{V}_s$ , while intersecting the plume. The altitude,  $z$ , is only adjusted between transects with the UAS outside the plume (measuring ambient or background concentrations).

Mass balance estimation techniques ~~such~~ require knowledge of the wind speed perpendicular to the direction of travel  
370 (transect crosswind). Optimally, each transect would therefore be perpendicular to the mean horizontal wind direction ( $\bar{\mathbf{u}}$ ), but local topography, changing wind fields, and flight safety considerations often result in an angle other than  $90^\circ$  between  $\mathbf{V}_s$  and  $\mathbf{u}$ . Therefore, it is important to first define a unit vector,  $\hat{n}$ , perpendicular to the direction of travel.

$$\begin{cases} \|\hat{n}\| = n_x^2 + n_y^2 = 1 \\ \mathbf{V}_s \cdot \hat{n} = V_x n_x + V_y n_y = 0 \end{cases} \quad (3)$$

Equation 3 shows the system of equations used to calculate this unit vector-

375 ~~,  $\hat{n}$ , using the instantaneous horizontal UAS velocities  $V_x$  and  $V_y$  are the instantaneous UAS velocities~~ defined previously. The transect crosswind, a measure of windspeed perpendicular to the UAS transect, is  $(\mathbf{u} \cdot \hat{n})$ . Maintaining a constant heading and horizontal velocity during flights proved difficult during periods of irregular and shifting winds. Direct measurements of  $\mathbf{u}$  and  $\mathbf{V}_s$  are variable between samples so that  $\hat{n}$  is required to constrain the flux calculation with respect to each transect.

Each of the  $K$  horizontal transects gets processed individually to calculate the intermediate transect-integrated flux  $f_k$   
380 (equation 4). ~~This is~~, the horizontal integral of the ~~measurements samples~~ along each transect ~~with~~ (units of mass flux rate per ~~unit vertical distance~~(vertical distance,  $\text{kg s}^{-1} \text{m}^{-1}$ ).

$$f_k = \eta \sum_{i=0}^{n-1} \rho_i (\chi - \chi_0)_i (\mathbf{u} \cdot \hat{n})_i \Delta s_i = \sum_{i=0}^{n-1} (C - C_0)_i (\mathbf{u} \cdot \hat{n})_i \Delta s_i \quad (4)$$

$\eta \rho (\chi - \chi_0) = (C - C_0)$  is the background-adjusted ~~mixing ratio~~ mole fraction,  $\Delta s = |\mathbf{V}_s| \Delta t = \sqrt{V_x^2 + V_y^2}$  is the distance between samples ( $\Delta t \approx 1 \text{ s}$ ), and  $\rho$  and  $\eta$  are defined previously.

385 The total flux,  $F_{tot}$ , is then calculated through integrating the sum of  $f_k$  and the vertical distance between physically adjacent transects,  $\Delta z_k$  (equations 5 and 6).

$$\Delta z_k = \begin{cases} |\bar{z}_{k+1} - \bar{z}_k| / 2 + 3 |\bar{z}_k| / 4 & \bar{z}_k = \min(\bar{z}_0, \dots, \bar{z}_{K-1}) \\ |\bar{z}_{k-1} - \bar{z}_k| & \bar{z}_k = \max(\bar{z}_0, \dots, \bar{z}_{K-1}) \\ (|\bar{z}_{k-1} - \bar{z}_k| + |\bar{z}_{k+1} - \bar{z}_k|) / 2 & \text{otherwise} \end{cases} \quad (5)$$

$$F_{tot} = \sum_{k=0}^{K-1} (f_k \Delta z_k) \quad (6)$$



390 For most transects,  $\Delta z_k$  ranges from the midpoint distance between the previous, lower altitude transect up to the midpoint  
between the next, higher altitude transect. Adjustments to the vertical integral step  $\Delta z_k$  are taken at the bottom and top  
traverse to account for extrapolation to the ground and above the flight pattern. The UAS is not capable of sampling all the  
way to ground level, however we expect the plume flux to decrease nonlinearly to zero at the ground, and we extrapolate below  
the lowest flight transect by assuming a constant mixing ratio and wind speed between the lowest transect and 75% of the  
395 distance to ground. This choice of integral quadrature corresponds to a logarithmic vertical profile for the transect-integrated  
flux  $f$  below level  $z$ ,  $f = f_0 \ln(z/z_0)$ , with  $z_0 = 0.018z$ . In the absence of tall trees, power lines, or other obstructions, the  
lowest flight transect typically lies between 2-4 m above ground (including the UAS mast), and the assumed  $z_0$  therefore ranges  
between about 4 and 7 cm. Extrapolation at the top edge of the plume can be more complicated, but ideally, the uppermost  
flight transect will lie above the plume so that a linear interpolation can adequately account for the top of the plume profile.  
400 However, some flight patterns (e.g., 9) may not completely span the possible vertical extent of the plume, and in these isolated  
cases we adopt a conservative approach by assuming a constant mixing ratio and wind above the transect altitude, extending  
only to a height defined by half the vertical distance between the top two transects. Typically, this extrapolation amounts to 2-4  
meters above the uppermost transect. A typical flight downwind of a natural gas point source is shown in figure 7. This flight  
is composed of eleven horizontal transects over a period of approximately 11 min. The transects were flown approximately  
405 130 m downwind (roughly south-southeast) of the methane point source with a known emission rate of  $3.42 \pm 0.01 \text{ kg h}^{-1}$   
(El Abbadi et al. (2023)).

### 2.3 Precision and Uncertainties

~~Figure 4 presents the distribution of and baseline estimate residuals ( $\epsilon_0 = \chi_0 - \tilde{\chi}_{bg}$ ) taken from two test flights downwind of  
known natural gas point sources. The  $3\sigma$  confidence interval (99.7%) is approximately for and for enhancement detection.~~

410 Table 1 gives the measurement uncertainties for the major components of the UAS.

~~Table 1 gives the measurement uncertainties for the major components of the UAS. Errors are calculated using the standard  
equation (7) described in Taylor (1996) for an arbitrary measured variable,  $q$ .~~

$$\delta q(x, \dots, z) = \sqrt{\left(\frac{\partial q}{\partial x}\right)^2 \delta x^2 + \dots + \left(\frac{\partial q}{\partial z}\right)^2 \delta z^2} \quad (7)$$

~~The precision on the baseline estimate and associated uncertainties for each sensor lead to an estimated lower quantification  
threshold of during standard flight conditions~~ transect-integrated flux,  $f_k$ , given in equation 4 is a function of the background-adjusted  
415 concentration ( $C - C_0$ ), windspeed perpendicular to UAS curtain, and the distance between transect samples ( $\Delta s$ ). Each of  
these terms introduces an error on  $f_k$  as defined in equations 8 through 10.

The uncertainty on the background-adjusted concentration,  $C$ , is dependent on the calculated air density ( $\rho = M_{air} P / (RT) \text{ kg m}^{-3}$ ),  
measured hydrocarbon concentration ( $\chi$ ), estimated background ( $\chi_0$ , see section 2.3), and the uncertainty associated with each  
420 value (see table 1).

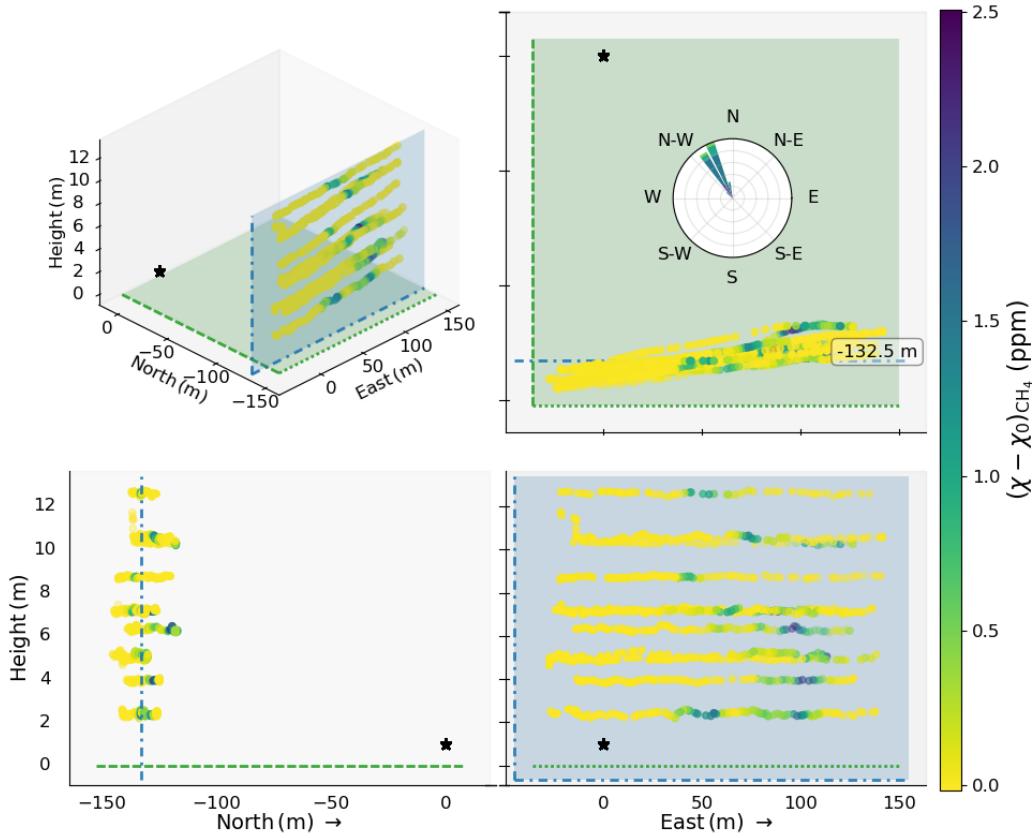


**Figure 7.** Plume transect flight pattern viewed from east (bottom left), south (bottom right), and from above (top right). Approximate source location marked with black square. The windrose plot (top left) shows the Earth-fixed wind in the horizontal direction. Estimated  $\text{CH}_4$  emission rate from UAS is  $4.15 \pm 1.11 \text{ kg h}^{-1}$

(compare to metered emission rate of  $3.52 \pm 0.01 \text{ kg h}^{-1}$ )

$$\begin{aligned}
 \delta(C - C_0) &= \eta \sqrt{\rho^2 \delta(\chi - \chi_0)^2 + (\chi - \chi_0)^2 \delta\rho^2} \\
 &= \eta M_{air} / R \sqrt{(P/T)^2 [\delta\chi + \delta\chi_0] + (\chi - \chi_0)^2 [(\delta P/T)^2 + (P\delta T/T^2)^2]}
 \end{aligned} \tag{8}$$

### 3 Analysis

Note that the uncertainty on the estimated  $\chi_0$  is calculated independently for each flight.

Table 1.

Sensor	Measurement	Uncertainty	Units	Variable
TWS	Pressure	1000	Pa	$\delta P$
TWS	Temperature	2	C	$\delta T$
TWS	Wind Speed	0.2	m/s	$\delta u_m, \delta v_m$
M600P GNSS	Horizontal Velocity	0.05	m/s	$\delta V_x, \delta V_y$
M600P IMU	Heading (Yaw)	0.05	rad	$\delta \phi$
M600P IMU	Pitch, Roll	0.017	rad	$\delta \theta, \delta \psi$
MIRA Pico	Methane	1.0	ppb	$\delta \chi_{CH_4}$
MIRA Pico	Ethane	0.5	ppb	$\delta \chi_{C_2H_6}$
RPi RTC	Timestamp	100	ms	$\delta(\Delta t)$
Pipeline*	Methane Background	5.0	ppb	$\delta \chi_{0,CH_4}$
Pipeline*	Ethane Background	1.0	ppb	$\delta \chi_{0,C_2H_6}$

425 The crosswind uncertainty is dependent on the static-frame horizontal windspeed ( $\mathbf{u}$ ) calculated as described in section 2.2 with the full uncertainty propagation given in section B1. While the crosswind is dependent the unit vector ( $\hat{n}$ ), the conservative upper limit approximation for cross wind is given on the equation 9.

$$\delta(\mathbf{u} \cdot \hat{n}) = \sqrt{n_y^2 \delta u^2 + n_x^2 \delta v^2} \approx \sqrt{\delta u (u_m, \phi, V_x)^2 + \delta v (v_m, \phi, V_y)^2} \quad (9)$$

430 The final parameter in  $\delta f_k$  is the separation between sample along the transect,  $\Delta s$ , which is dependent on the UAS horizontal velocity ( $V_h = \sqrt{V_x + V_y}$ ), sampling rate ( $\Delta t = 1$  Hz), and the associated uncertainties as shown in equation 10.

$$\delta(\Delta s) = \sqrt{\delta V_h^2 \Delta t^2 + V_h^2 \delta(\Delta t)^2} = \sqrt{[(V_x \delta V_x)^2 + (V_y \delta V_y)^2] (\Delta t / V_h)^2 + [V_x^2 + V_y^2] \delta(\Delta t)^2} \quad (10)$$

The calculated uncertainty on  $f_k$  is therefore calculated as shown in equation 11.

$$\delta f_k^2 = [\delta(C - C_0) (\mathbf{u} \cdot \hat{n}) \Delta s]^2 + [(C - C_0) \delta(\mathbf{u} \cdot \hat{n}) \Delta s]^2 + [(C - C_0) (\mathbf{u} \cdot \hat{n}) \delta(\Delta s)]^2 \quad (11)$$

435 The total source flux is the summation of each  $f_k$  multiplied by the corresponding  $\Delta z_k$ , as shown in equation 6. The vertical range of each independent transect is given in equation 5.  $\bar{z}_k$  is the average height of all samples within transect  $k$  and  $\delta(\Delta z) = \sigma_{z_k}$  is the uncertainty in altitude.

$$\delta F_{tot} = \sqrt{\delta f_k^2 \Delta z^2 + f_k^2 \delta(\Delta z)^2} \quad (12)$$

The measurement uncertainties detailed in equations 8 through 12 can be used to identify the major sources of uncertainty in source emission rate estimates.

440 While the minimum flux threshold will depend on the specific meteorological conditions and flight patterns during sampling, under favorable flight conditions with high solar insolation,  $2 \text{ m s}^{-1}$  mean windspeed, and a downwind plume cross-sectional area of  $100 \text{ m}^2$  (see Figure 5), the minimum source strength that can be quantified is on the order of  $0.0062 \text{ kg}(\text{CH}_4) \text{ h}^{-1}$  and  $0.0018 \text{ kg}(\text{C}_2\text{H}_6) \text{ h}^{-1}$ .

### 3 Results

445 This section gives an overview of multiple quantification flights between spring 2022 and Fall 2023. Section 3.1 details the results of multiple controlled releases using the system described in El Abbadi et al. (2023). Section 3.2 discusses measurements from various, smaller biogenic and thermogenic emission sources collected between winter 2021 and Fall 2023.

#### 3.1 Controlled Release Experiments

In Fall of 2022, the NMT team participated in a single-blind controlled release validation campaign in Casa Grande, Arizona, USA (Sherwin et al. (2023); El Abbadi et al. (2023)). While this validation campaign focused on larger-scale aircraft and satellite system validation, it was a unique opportunity to quantify the accuracy for this method of direct methane flux quantification. The UAS was deployed multiple times around the controlled release location during two separate, three-day validation trips: October 10–12 and November 14–16, 2022. Multiple flights at various times throughout the daily testing window (between 10:00 and 14:00 MST most days) measured concentrations downwind of the release stack.

455 ~~Due to battery life and charging limitations, the UAS typically can accommodate about one flight per hour. Additionally, the flux quantification method described in section 2.2 relies on relatively stable wind fields around the source, optimally between 2 and  $6 \text{ m s}^{-1}$ .~~ Suboptimal environmental conditions and unforeseen instrumentation issues resulted in the rejection of the majority October 2022 flights from the analysis process. The November 2022, 3-day campaign produced a total of 12 flights, 8 of which were during times of low-variability windfields and good flight conditions to allow for reliable flux quantification.

460 It is important to note that, at the time of this campaign, the UAS flight pattern and quantification method was still in active development. While the NMT team quantified and submitted flux estimates during the single-blind and partially-blinded phases of the unblinding process (described in El Abbadi et al. (2023)), the final unblinded metered emissions were invaluable to debug and update the initial quantification process, ultimately leading to the numerical integration outlined in section 2.2. Here, we present the analysis of the quantification results informed by the unblinded, ~~ground-truth-methane~~ ground-truth methane flow rates.

Figure 8 shows the comparison between UAS-calculated flux and the corresponding unblinded metered emissions from 8 independent November 2022 flights. The metered rates, taken to be the ground truth emission rates, range from 1.7 to  $1500 \text{ kg h}^{-1}$ . This broad range of emission rates highlights the system's dynamic range and the fitted linear regression shows the quality of emission estimates compared to the one-to-one agreement with metered rates (dotted line). Our method of flux

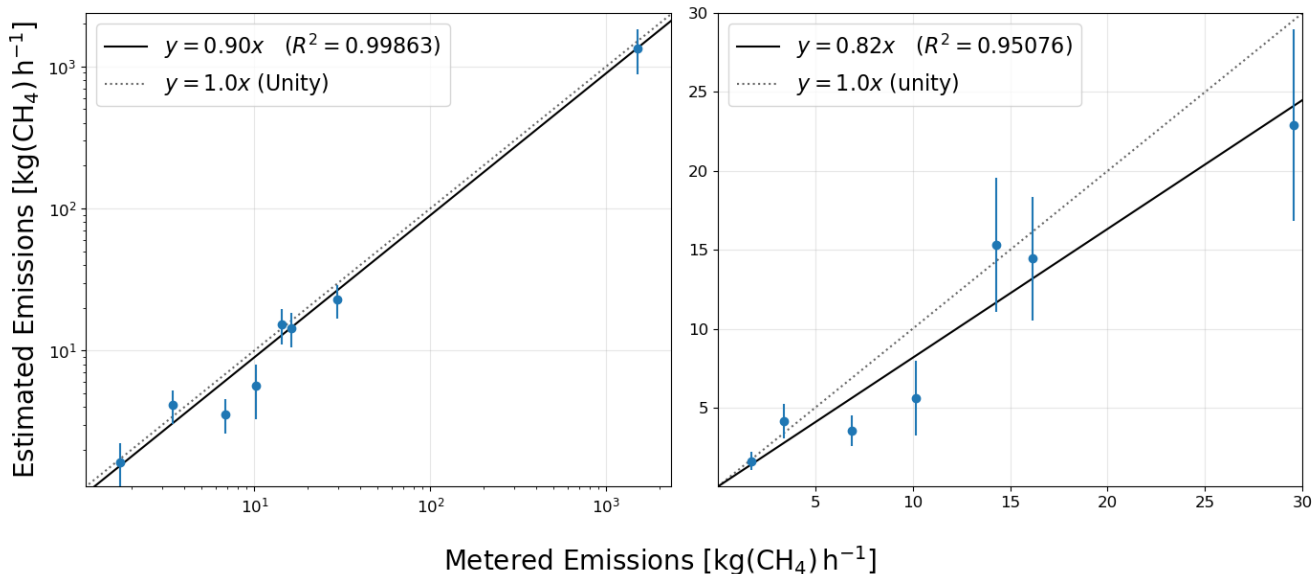


**Figure 8.** Comparison of UAS CH<sub>4</sub> flux calculation versus Metered Emissions reported by El Abbadi et al. (2023) and Sherwin et al. (2023). Both plots show 8 individual flights during the November 2022 field campaign with 2σ error bars. Linear regression fit shown as solid line for comparison with the idealized one-to-one fit corresponding to perfect agreement between UAS and Metered data (dotted line). *Left* Logarithmic plot highlighting UAS’s large dynamic range. *Right* Linear plot focused on emission rates below detection limits of most aircraft quantification methods; linear regression fit does not include emission rates above 100 kg h<sup>-1</sup>.

470 quantification shows reasonable agreement with the expected emission rates above 1 kg h<sup>-1</sup>. However, the results suggest a **systematic** an underestimation of the emissions which is not correlated to number of transects or windspeeds during flights. This may be due to the limited flight time and under-sampling the downwind plume with the UAS. One interpretation of these results is that our field measurements could represent a reasonable lower bound to the true emission rate of the source.

### 3.2 **Other** Targeted Point and Distributed Sources

475 The deployment strategy for this UAS is designed to quantify emissions from targeted local sources such as O&NG wells and manure storage/biogenic lagoons. With a limited operational distance and flight time, larger distributed sources (such as large-scale dairies and agricultural centers) are difficult to properly quantify using the numerical integration technique described in section 2.2. However, smaller-scale municipal waste facilities with heterogeneous emission profiles can be quantified as long as the UAS is able to fully, and repeatedly, transect the complex and irregular plumes downwind of the facility.

#### 480 3.2.1 **Municipal Waste Facility**

During the course of system development and testing, the UAS was deployed around a local Municipal Waste Facility (MWF) in Socorro, NM. This location serves a county population of approximately 16,300 with multiple cells over an area of 45 hectares.

Larger facilities studied by Olaguer et al. (2022) and Lan et al. (2015) reported emission rates between 85 and  $> 2000 \text{ kg h}^{-1}$ ; this much smaller local facility, however, was expected to emit at rates less than  $10 \text{ kg h}^{-1}$  (Olaguer et al. (2022); Bogner and Matthews (2003)). The low emission rate and temporal heterogeneity, likely due to changes in cell activity, is evident across the multiple visits between Spring 2022 and Summer 2023. The flight path from one such flight can be seen in figure 9.

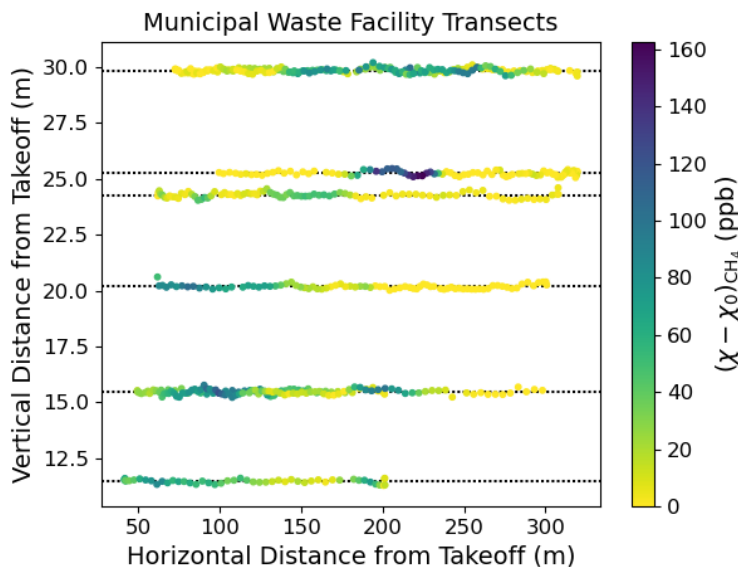


**Figure 9.** Example flight, split into individual transects, from landfill in New Mexico. The landfill itself is composed of activate and inactive cells distributed over an area of approximately 45 ha, resulting in a non-uniform downwind plume profile. Comparison with localized ‘point source’ presented in figure 7, longer horizontal transects across a wider vertical range are required to measure the multiple distributed and highly variable emitters. Estimated flux rate for this flight is  $1.33 \pm 0.58 \text{ kg h}^{-1}$ .

In comparison to flights downwind of point sources such as O&NG wells or controlled NG releases (figure 7), the flight pattern in figure 9 was positioned about 0.5 km downwind of the source and involved plume transects up to  $\sim 500 \text{ m}$  long, and over an altitude range of up to 50 m. In addition, the methane enhancements are about a factor of 10 lower than in figure 7, and the plume is distributed over a larger area and centered at a higher altitude. Nevertheless, the overall plume structure allows for the same flux analysis as discussed for the localized NG point sources above. The measured methane emission rate for this flight was  $1.12 \pm 0.67 \text{ kg h}^{-1}$   $1.33 \pm 0.58 \text{ kg h}^{-1}$ .

### 3.2.2 Orphan Well

During April 2023, the UAS was also deployed around an ‘orphaned well’ located in Hobbs, New Mexico, USA. This site has been out-of-use for more than two decades and was in the initial phase of being plugged when visited in April 2023. A detailed analysis of data from this field campaign is presented in Follansbee et al. (2024). The observed plume structure was similar to

that shown in figure 7, but mean wind speeds were much larger and methane plume enhancements were ~400 ppb, roughly between the range of plume enhancements shown in figures 7 and 9. Three downwind flights yielded consistent fluxes in the range of 0.3 to 0.4 kg h<sup>-1</sup> (Follansbee et al. (2024)).

### 500 3.2.3 Wastewater Treatment Plant

Wastewater Treatment Plants (WWTPs) are a known source of biogenic methane emissions via biodegradation of pollutants by anaerobic bacteria (Song et al. (2023)). The small town of Socorro, NM has a local Wastewater Treatment plant that processes less than one million gallons per day (MGD) so that its contribution to anthropogenic methane is relatively quite low (when compared to O&NG and agricultural operations). However, the low emission rate of this location was useful for testing of the UAS's lower detection and quantification limits.

A timeseries of measured CH<sub>4</sub> and C<sub>2</sub>H<sub>6</sub> concentrations from a short flight in August 2023 is shown in figure 10. The CH<sub>4</sub> and C<sub>2</sub>H<sub>6</sub> detection limit (calculated from the background fit residual 3σ confidence interval, see section 2.3) is overlaid on the timeseries shown in figure 9. While the in-plume CH<sub>4</sub> concentration levels peak at around 40 ppb, ~~the measured no corresponding C<sub>2</sub>H<sub>6</sub> levels do not exceed the sensor's noise floor of enhancements are detected~~ while passing through the plume. The lack ~~of any a~~ correlation between C<sub>2</sub>H<sub>6</sub> ~~& and~~ CH<sub>4</sub> is strong evidence that the measured plume is from anaerobic digestion at the WWTP and is not contaminated by another source. However, it is important to note that weaker source strengths lead to a decrease in the signal-to-noise ratio so that C<sub>2</sub>H<sub>6</sub> from thermogenic sources may not be detectable. This is shown visually at the bottom of figure 10 where the expectation C<sub>2</sub>H<sub>6</sub> timeseries for 10% and 5% C<sub>2</sub>H<sub>6</sub>:CH<sub>4</sub> thermogenic plumes are modelled with respect to the measured CH<sub>4</sub> timeseries. While the C<sub>2</sub>H<sub>6</sub> signal for the 10% thermogenic mixture peaks above the detection threshold (1.5 ppb in this dataset), the 5% mixture is barely visible above the noise floor. However, it is important to note that weaker source strengths lead to a decrease in the signal-to-noise ratio so that C<sub>2</sub>H<sub>6</sub> from thermogenic sources may not be detectable. This is shown visually at the bottom of figure 10 where the expectation C<sub>2</sub>H<sub>6</sub> timeseries for 10% and 5% C<sub>2</sub>H<sub>6</sub>:CH<sub>4</sub> thermogenic plumes are modelled with respect to the measured CH<sub>4</sub> timeseries. While the C<sub>2</sub>H<sub>6</sub> signal for the 10% thermogenic mixture peaks above the detection threshold (1.5 ppb in this dataset), the 5% mixture is barely visible above the noise floor.

515  
520

### 3.3 Source Attribution

As discussed in Section 1, simultaneous measurements of both CH<sub>4</sub> and C<sub>2</sub>H<sub>6</sub> is useful for source classification as either biogenic or thermogenic. In addition, there are varying ratios of trace hydrocarbons found in thermogenic natural gas sources, and C<sub>2</sub>H<sub>6</sub> is the second-most dominant compound in refined natural gas (Peischl et al. (2018); Hodnebrog et al. (2018); Kutcherov and Krayushkin (2010); Glasby (2006); Space Studies Board et al. (2019); Solomon et al. (2007); Hansen et al. (2000); Meyer et al. (2022)). Therefore, the ratio of C<sub>2</sub>H<sub>6</sub> to CH<sub>4</sub> can be used to estimate the percentage of non-methane compounds in an O&NG plume and distinguish between sources.

Figure 11 shows the ratio of measured C<sub>2</sub>H<sub>6</sub> and CH<sub>4</sub> ~~mixing ratios mole fraction~~ from five different field measurements around various sources, including the municipal waste facility discussed in section 3.2.1. Multiple downwind plume measure-

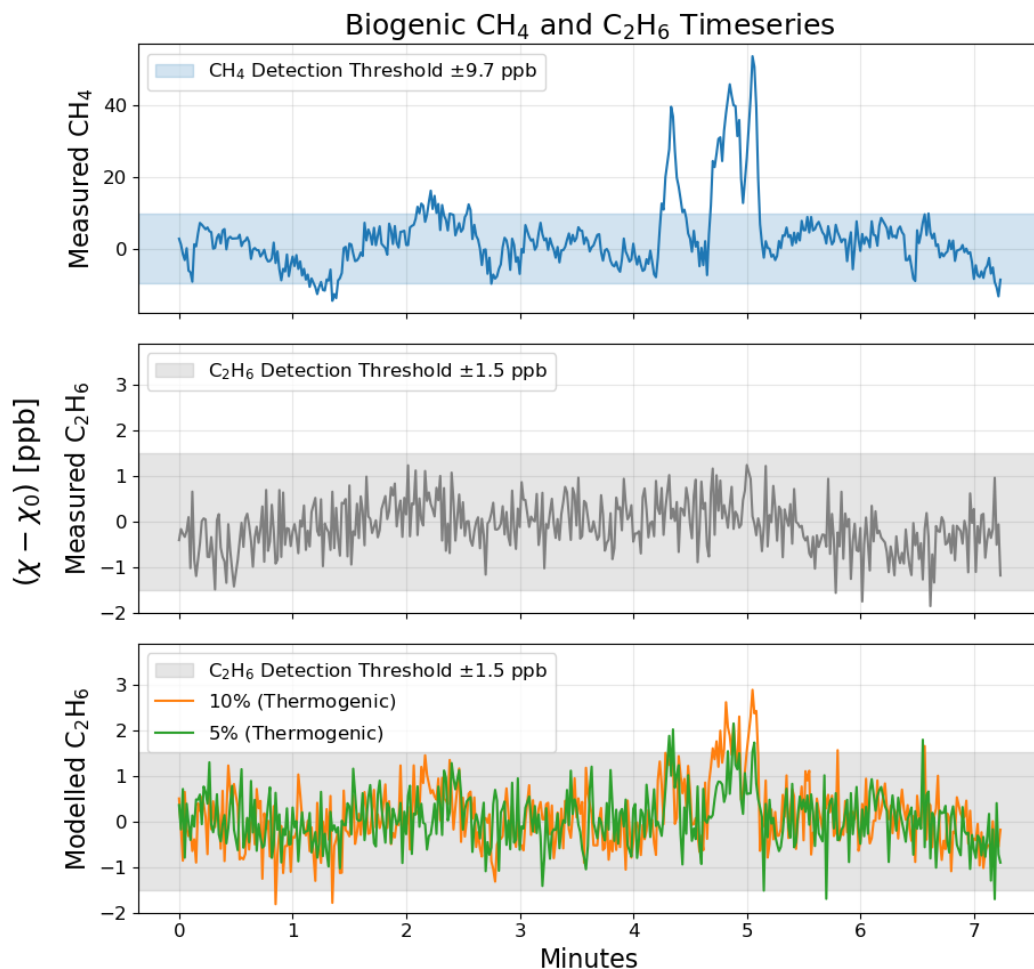


**Figure 10.** (Top and Middle) Timeseries of measured and background subtracted  $\text{CH}_4$  and  $\text{C}_2\text{H}_6$  concentrations (section 2.3) from a flight downwind of the City of Socorro wastewater treatment plant in August 2023. (Bottom) Expectation  $\text{C}_2\text{H}_6$  timeseries if measured  $\text{CH}_4$  plume (Top) was thermogenic with 10% and 5%  $\text{C}_2\text{H}_6:\text{CH}_4$  ratios. The mean winds were  $\sim 5 \text{ m s}^{-1}$  and the solar insolation corresponded to stability class “B” due to partial cloud coverage (Seinfeld and Pandis (2006); Woodward (1998)). The plume was intercepted on two transects separated by about 40 s, as seen in the  $\text{CH}_4$  timeseries (top) about 4-5 minutes into the flight. No corresponding  $\text{C}_2\text{H}_6$  enhancements were measured indicating that the plume is biogenic (compare with expectation thermogenic  $\text{C}_2\text{H}_6$  timeseries). Estimated  $\text{CH}_4$  emission rate of  $0.061 \pm 0.032 \text{ kg h}^{-1}$ .

530 ments showed a negligible  $\text{C}_2\text{H}_6$  content ( $\ll 0.2\% \left| \frac{\Delta \text{C}_2\text{H}_6}{\Delta \text{CH}_4} \right| < 0.2\% \left| \frac{\text{C}_2\text{H}_6}{\text{CH}_4} \right|$ ) from this biogenic source. Consistent with figure 9, the magnitude of plume  $\text{CH}_4$  from the MWF is much lower in comparison to the thermogenic methane sources we have sampled. Figure 12 highlights the dynamic range of the UAS, which is able to detect  $\text{CH}_4$  enhancements of as little as  $20 \text{ ppb s}^{-1}$  (after baseline-background removal, Section 2.3). Additionally, the UAS has demonstrated the ability to



## Background-Subtracted C<sub>2</sub>H<sub>6</sub> to CH<sub>4</sub> Ratios

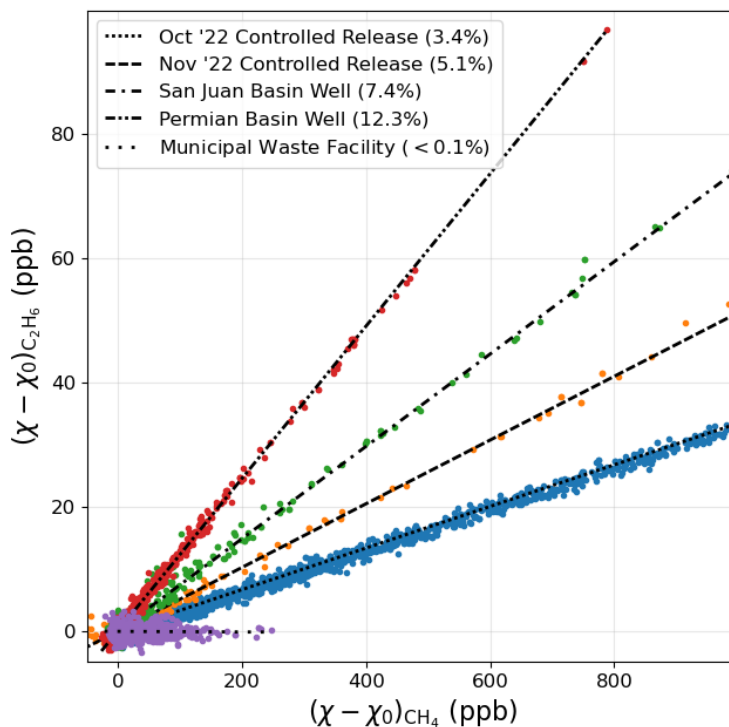


**Figure 11.** Ethane & Methane enhancement ratios from multiple independent field tests at different sites. *October and November 2022 Controlled Releases:* are two independent multi-day field campaigns in Casa Grande, AZ during a controlled NG release. *San Juan Basin Well:* Multiple flights near an active well-head in Cuba, NM. *Permian Basin Well:* three independent flights downwind of an orphan well in Hobbs, NM, *Municipal Waste Facility* is a relatively small waste disposal location near Socorro, NM.

measure much larger concentrations of more than 40,000 ppm (empirically determined based on MIRA Pico saturation levels during AZ validation flights).

The two different controlled release campaigns in Fall 2022 were about one month apart, and these data are segregated in figure 12. The measured percentages are in agreement with the contemporaneous CH<sub>4</sub> concentration measurements reported by the controlled release team (El Abbadi et al. (2023)). The same ratio of C<sub>2</sub>H<sub>6</sub> to CH<sub>4</sub> was measured across all flights during the first release and similarly during the second campaign, though the ethane content was noticeably different during the second campaign.

Emissions of unrefined NG from the orphan well discussed in section 3.2.2 contained a smaller fraction of CH<sub>4</sub> due to the presence of other compounds such as H<sub>2</sub>S, so that it is incorrect to approximate the C<sub>2</sub>H<sub>6</sub> ratio in figure 11 as the non-CH<sub>4</sub> percentage. However, this unique C<sub>2</sub>H<sub>6</sub>:CH<sub>4</sub> ratio was consistent across all orphan well flights, and in good agreement with ground-based systems deployed at the same site (Follansbee et al. (2024)); larger ethane content is due to the unrefined natural

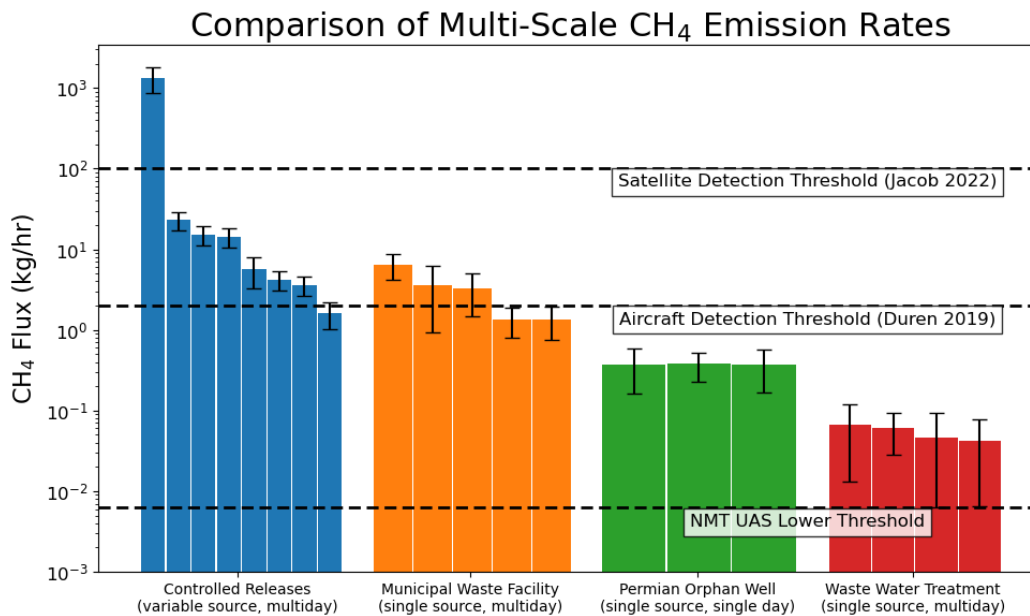


**Figure 12.** Comparison of estimated Methane flux from various anthropogenic sources. The UAS has a large dynamic range capable of quantifying emission rates from smaller sources (less than  $1 \text{ kg h}^{-1}$ ). Horizontal dashed lines show the absolute lowest detection limits for satellite and aircraft quantification methods (Jacob et al. (2022); Duren et al. (2019)) with respect to the estimated lower limit of this system ( $\sim 0.007 \text{ kg h}^{-1}$ , see section 2.3)

545 gas seeping from the unused well. (Stolper et al. (2018)). Furthermore, measurements of unrefined NG from a leaking O&NG  
 well in the San Juan Basin, obtained in October 2023, showed a distinct ratio from that of the orphan well from the Permian  
 Basin. The San Juan Basin is primarily a coal producing region and therefore has a noticeably lower  $\text{C}_2\text{H}_6$  content compared  
 to the Permian Basin, the latter region being primarily composed of oil. Thus, each of the sources shown in Figure 12 had a  
 unique and consistent  $\text{C}_2\text{H}_6$  ratio which can be used to characterize and differentiate multiple sources based on this percentage.  
 550 This is in agreement with the findings of Meyer et al. (2022).

#### 4 Conclusions

Our results demonstrate the capabilities of this integrated UAS package, along with associated flight strategies and data analysis  
 methodologies, to quantify and characterize methane ~~emitters across a range of spatial scales (point to)~~ of point and distributed  
~~emission sources~~. Through direct, in situ measurements of  $\text{CH}_4$  ~~mixing ratios concentrations~~ and vector winds ~~within the~~  
 555 ~~downwind plumes downwind~~ of target sources, ~~this system the UAS~~ can be used to ~~robustly quantify emission source strengths~~  
~~quantify emission rates~~ spanning more than three orders of magnitude. ~~Figure 12 presents a summary of flux measurements~~  
~~from different sources, ranging from large ( ) emissions in controlled release experiments, to the very low emissions ( ) observed~~

560 from a local WWTP. Large error bars on the four independent WWTP flights are consistent with the error associated for other low-emission. As noted in the figure, our UAS has the capability to quantify emission rates up to and above the lower limits of satellite and aircraft. The lower bound limit for CH<sub>4</sub> monitoring systems; thus it is useful for contemporaneous source quantification to help constrain and bridge the gap between ground-based and top-down measurement systems. The lower measurement bound for methane fluxes flux measurements is estimated to be  $\sim 0.007 \text{ kg h}^{-1}$ , and it is determined primarily by the precision of the methane measurement concentration measurements and uncertainties associated with the background determination and plume enhancement. determining the background levels with respect to variable plume enhancements.

565 Environmental conditions largely dictate the plume dispersion and transport with respect to a target source; optimal downwind distances and transect velocities during flight are highly dependent on insolation and windspeed/direction. The results from the controlled releases shown in figure 8 and table B1 were obtained during daytime periods of relatively steady winds and low cloud coverage (high solar insolation leading to large vertical mixing). In all cases, the measured emission rates showed reasonable agreement with metered flow rates, generally within  $1\sigma$  error. However, the results suggest the potential for a  
570 small systematic underestimation of emissions across all scales, depending on environmental conditions. This underestimation may arise from limitations on the horizontal extent or vertical distribution of transects during each flight, resulting in an under-sampling of the continuous emission plume. Therefore, UAS flux quantification may represent an effective lower-bound value for the true emission rate. It is important to note that the results in section 3.1 were informed by the fully unblinded metered rates whereas the aforementioned aircraft systems used fully blinded or partially unblinded data for the reported  
575 estimates (El Abbadi et al. (2023); Sherwin et al. (2023)).

The primary limitations of our UAS measurement approach are related to meteorological conditions. Optimum mean wind speeds are in the range  $2\text{-}6 \text{ m s}^{-1}$ . Wind speeds below  $2 \text{ m s}^{-1}$  have been shown to produce less reliable fluxes due to higher variability in the plume position and shape, while winds above  $6 \text{ m s}^{-1}$  are too strong for safe flights with this UAS. The steadiness of wind directionality can also be a factor, although it is a much less severe constraint than speed provided that  
580 the flight pattern is sufficiently wide to intersect the plume on every transect. Proper deployment also requires access for takeoff and landing within 1 km of the source, and the target source's location must also be known to within a few kilometers. While successful deployment and flux quantification is constrained to a specific range of environmental conditions, the UAS offers a relatively simple method of deployment for quantifying emitters that would otherwise be difficult or impossible for other monitoring techniques to access or detect. Thus, although this system is not optimized for wide-area surveys, it is well  
585 suited for site quantification of known sources such as O&NG wells or processing facilities, small dairies and municipal waste facilities, and wastewater treatment plants.

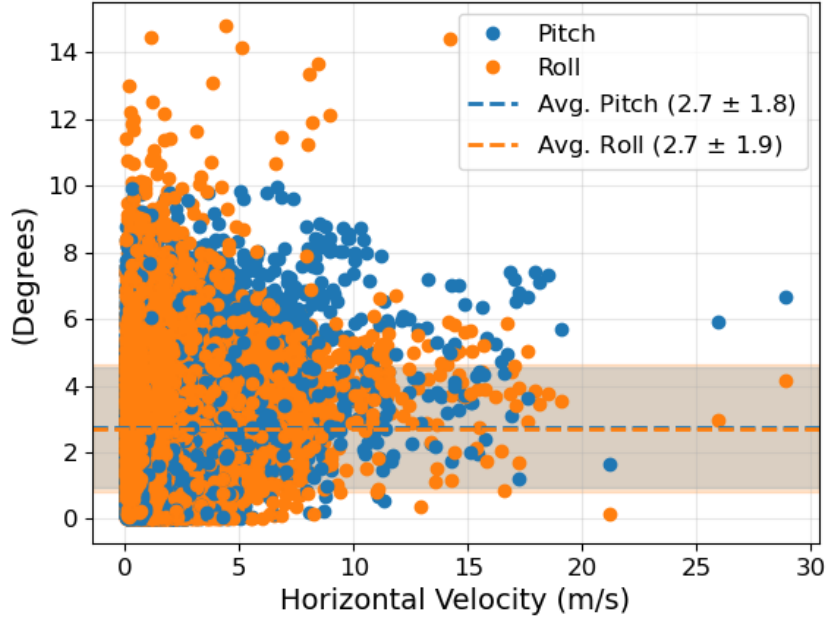


**Figure A1.** Instantaneous UAS Pitch and Roll versus horizontal velocity from all flights presented in figure 12 and table B1 (> 13,500 samples). Plot contains all samples prior to filtering and transect processing as described in section 2.2.

**Appendix A:** [Supplemental Information](#)

**Appendix B:** [Supplemental Equations](#)

**B1** [Static Vector Wind Uncertainty](#)

$$590 \quad \delta u = \sqrt{\left(\frac{\partial u}{\partial u_m}\right)^2 \delta u_m^2 + \left(\frac{\partial u}{\partial \phi}\right)^2 \delta \phi^2 + \left(\frac{\partial u}{\partial V_x}\right)^2 \delta V_x^2} \quad (\text{B1})$$

$$\delta v = \sqrt{\left(\frac{\partial v}{\partial v_m}\right)^2 \delta v_m^2 + \left(\frac{\partial v}{\partial \phi}\right)^2 \delta \phi^2 + \left(\frac{\partial v}{\partial V_y}\right)^2 \delta V_y^2} \quad (\text{B2})$$

$$\frac{\partial u}{\partial u_m} = \cos(\phi) \quad \frac{\partial u}{\partial \phi} = -u_m \sin(\phi) + v_m \cos(\phi) \quad \frac{\partial u}{\partial V_x} = 1 \quad (\text{B3})$$

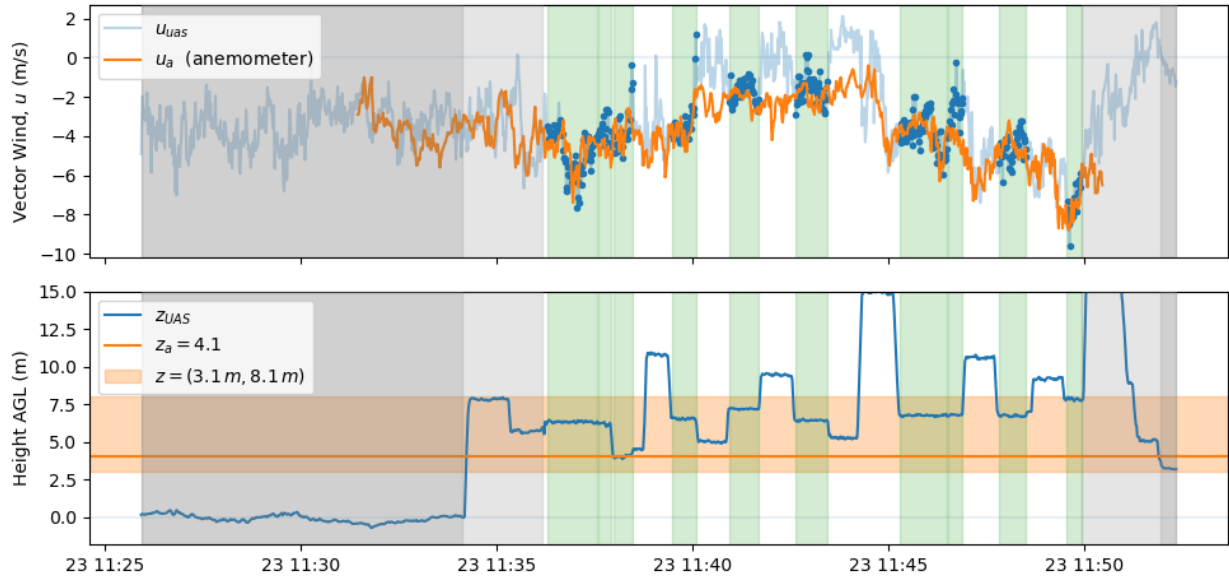


**Figure A2.** (Top) Comparison of vector wind ( $u$ ) from UAS adjustment (section 2.2) with directional ground anemometer aligned to the west. (Bottom height of UAS above ground level (blue) with respect to anemometer (orange). Highlighted regions depict steady/level transects within 20 m horizontal distance from the fixed anemometer.)

$$595 \quad \frac{\partial v}{\partial v_m} = \cos(\phi) \quad \frac{\partial v}{\partial \phi} = -v_m \sin(\phi) - u_m \cos(\phi) \quad \frac{\partial v}{\partial V_y} = 1 \quad (\text{B4})$$

*Competing interests.* The contact author has declared that none of the authors has any competing interests.

*Acknowledgements.* Support for instrumentation and [UAV-UAS](#) equipment provided in part by the New Mexico Tech Office of Research. This project has benefited from collaborations with the New Mexico Bureau of Mines, the New Mexico Petroleum Recovery Research Center, and Los Alamos National Laboratory. We thank the NMT Facilities Management Office for their support of field measurements during the course of this project.

Special thanks to operators of the controlled release in Casa Grande, AZ; recognizing the team members who contributed to field operations during the October and November 2022 testing periods and to processing the ground-truth data that was provided (in alphabetical order by last name): Adam R. Brandt, Philippine M. Burdeau, Yuanlei Chen, Zhenlin Chen, Sahar H. El Abbadi, Jeffrey S. Rutherford, Evan D. Sherwin. From Rawhide Leasing (operating the gas equipment): Mike Brandon, S.M.

**Table B1.** Table measured emission rates from various source types shown in figure 12. Presented error ranges are the  $\pm 1\sigma$  bounds calculated from sensor uncertainties and background estimation as described in section 2.2.

Source Type	$F_{tot} [\text{CH}_4]$ ( $\text{kg h}^{-1}$ )	$F_{tot} [\text{C}_2\text{H}_6]$ ( $\text{kg h}^{-1}$ )	$\langle  u  \rangle$ ( $\text{m s}^{-1}$ )	$\langle \angle u \rangle$ (deg)	$\langle T \rangle$ (C)	$\langle P \rangle$ (hPa)	$K$	Duration (min)	Date
Controlled Release	1342.624 [ 875.334, 1809.914]	25.831 [ 16.888, 34.774]	2.6	391.1	12.7	969.9	10	11:24	11/15/2022
Controlled Release	22.904 [ 16.862, 28.946]	1.475 [ 1.044, 1.906]	4.3	318.9	11.2	974.8	7	12:46	11/16/2022
Controlled Release	15.300 [ 11.060, 19.540]	0.962 [ 0.681, 1.243]	4.5	363.9	15.1	974.2	7	14:00	11/16/2022
Controlled Release	14.438 [ 10.498, 18.378]	0.876 [ 0.617, 1.135]	3.4	325.5	16.8	968.0	8	13:03	11/15/2022
Controlled Release	5.630 [ 3.261, 7.999]	0.345 [ 0.192, 0.498]	1.6	334.2	11.4	970.6	12	16:59	11/15/2022
Controlled Release	4.154 [ 3.040, 5.268]	0.264 [ 0.168, 0.360]	5.1	333.5	12.8	974.9	11	17:59	11/16/2022
Controlled Release	3.564 [ 2.606, 4.522]	0.218 [ 0.124, 0.312]	4.6	356.2	13.8	974.9	6	10:45	11/16/2022
Controlled Release	1.629 [ 1.035, 2.223]	0.100 [ 0.057, 0.143]	3.5	333.8	15.3	968.8	15	18:44	11/15/2022
Municipal Waste Facility	6.476 [ 4.187, 8.765]	-	3.8	354.2	19.7	862.7	10	12:19	8/31/2022
Municipal Waste Facility	3.625 [ 0.944, 6.306]	-	4.8	337.9	18.9	862.7	8	11:19	8/31/2022
Municipal Waste Facility	3.279 [ 1.473, 5.085]	-	7.1	326.8	26.1	858.2	6	11:56	8/10/2023
Municipal Waste Facility	1.336 [ 0.806, 1.866]	-	3.5	324.0	24.2	856.6	6	15:29	6/29/2023
Municipal Waste Facility	1.331 [ 0.744, 1.918]	-	5.5	318.3	7.6	867.5	6	11:13	10/28/2022
Permian Orphan Well	0.374 [ 0.165, 0.583]	0.085 [ 0.021, 0.149]	9.4	218.9	22.1	886.1	4	05:19	4/19/2023
Permian Orphan Well	0.378 [ 0.230, 0.526]	0.105 [ 0.067, 0.143]	5.9	182.6	16.7	886.7	11	11:44	4/19/2023
Permian Orphan Well	0.368 [ 0.170, 0.566]	0.089 [ 0.038, 0.140]	5.8	209.3	17.7	886.7	7	09:29	4/19/2023
Waste Water Treatment	0.066 [ 0.013, 0.119]	-	2.1	230.0	9.5	855.9	8	10:14	2/28/2023
Waste Water Treatment	0.061 [ 0.029, 0.093]	-	4.6	136.4	24.2	862.2	3	07:14	8/31/2023
Waste Water Treatment	0.046 [ 0.006, 0.093]	-	4.2	136.6	24.0	862.5	7	11:50	8/31/2023
Waste Water Treatment	0.042 [ 0.007, 0.077]	-	7.0	152.8	20.6	860.8	13	12:15	6/6/2023

## 605 **References**

- Aeris Technologies Inc: Aeris Technologies' PICO Series Mid-IR Laser-based Nitrous Oxide and Carbon Monoxide Gas Analyzer Operating Manual, 2019.
- Alexe, M., Bergamaschi, P., Segers, A., Detmers, R., Butz, A., Hasekamp, O., Guerlet, S., Parker, R., Boesch, H., Frankenberg, C., Scheepmaker, R. A., Dlugokencky, E., Sweeney, C., Wofsy, S. C., and Kort, E. A.: Inverse modelling of CH<sub>4</sub> emissions for 2010-  
610 2011 using different satellite retrieval products from GOSAT and SCIAMACHY, *Atmospheric Chemistry and Physics*, 15, 113–133, <https://doi.org/10.5194/acp-15-113-2015>, 2015.
- Anemoment LLC: Trisonica Mini User Manual, 2018.
- Anemoment LLC: World's Smallest & Lightest 3D Ultrasonic Anemometer, 2022.
- Barbieri, L., Kral, S., Bailey, S., Frazier, A., Jacob, J., Reuder, J., Brus, D., Chilson, P., Crick, C., Detweiler, C., Doddi, A., Elston, J.,  
615 Foroutan, H., González-Rocha, J., Greene, B., Guzman, M., Houston, A., Islam, A., Kemppinen, O., Lawrence, D., Pillar-Little, E., Ross, S., Sama, M., Schmale, D., Schuyler, T., Shankar, A., Smith, S., Waugh, S., Dixon, C., Borenstein, S., and De Boer, G.: Intercomparison of Small Unmanned Aircraft System (sUAS) Measurements for Atmospheric Science during the LAPSE-RATE Campaign, *Sensors*, 19, 2179, <https://doi.org/10.3390/s19092179>, 2019.
- Barchyn, T. E., Hugenholtz, C. H., and Fox, T. A.: Plume detection modeling of a drone-based natural gas leak detection system, *Elementa: Science of the Anthropocene*, 7, 41, <https://doi.org/10.1525/elementa.379>, 2019.
- Bel Hadj Ali, N., Abichou, T., and Green, R.: Comparing estimates of fugitive landfill methane emissions using inverse plume modeling obtained with Surface Emission Monitoring (SEM), Drone Emission Monitoring (DEM), and Downwind Plume Emission Monitoring (DWPEM), *Journal of the Air & Waste Management Association*, 70, 410–424, <https://doi.org/10.1080/10962247.2020.1728423>, 2020.
- Bhattacharya, R.: *Atmospheric Dispersion*, 2013.
- 625 Bogner, J. and Matthews, E.: Global methane emissions from landfills: New methodology and annual estimates 1980–1996, *Global Biogeochemical Cycles*, 17, 2002GB001 913, <https://doi.org/10.1029/2002GB001913>, 2003.
- Burgués, J. and Marco, S.: Environmental chemical sensing using small drones: A review, *Science of The Total Environment*, 748, 141–172, <https://doi.org/https://doi.org/10.1016/j.scitotenv.2020.141172>, 2020.
- Cheewaphongphan, P., Chatani, S., and Saigusa, N.: Exploring Gaps between Bottom-Up and Top-Down Emission Estimates  
630 Based on Uncertainties in Multiple Emission Inventories: A Case Study on CH<sub>4</sub> Emissions in China, *Sustainability*, 11, 2054, <https://doi.org/10.3390/su11072054>, 2019.
- Chen, J., Viatte, C., Hedelius, J. K., Jones, T., Franklin, J. E., Parker, H., Gottlieb, E. W., Wennberg, P. O., Dubey, M. K., and Wofsy, S. C.: Differential column measurements using compact solar-tracking spectrometers, *Atmospheric Chemistry and Physics*, 16, 8479–8498, <https://doi.org/10.5194/acp-16-8479-2016>, 2016.
- 635 Dà Jiāng Innovations: Matrice 600 Pro User Manual, 2018.
- Duren, R. M., Thorpe, A. K., Foster, K. T., Rafiq, T., Hopkins, F. M., Yadav, V., Bue, B. D., Thompson, D. R., Conley, S., Colombi, N. K., Frankenberg, C., McCubbin, I. B., Eastwood, M. L., Falk, M., Herner, J. D., Croes, B. E., Green, R. O., and Miller, C. E.: California's methane super-emitters, *Nature*, 575, 180–184, <https://doi.org/10.1038/s41586-019-1720-3>, 2019.
- El Abbadi, S., Chen, Z., Burdeau, P., Rutherford, J., Chen, Y., Zhang, Z., Sherwin, E., and Brandt, A.: Comprehensive evaluation of aircraft-  
640 based methane sensing for greenhouse gas mitigation, <https://eartharxiv.org/repository/view/5569/>, 2023.

- Etioppe, G. and Sherwood Lollar, B.: Abiotic Methane On Earth, *Reviews of Geophysics*, 51, 276–299, <https://doi.org/10.1002/rog.20011>, 2013.
- Federal Aviation Administration: Remote Pilot - Small Unmanned Aircraft Systems Airman Certification Standards, 2021.
- 645 Follansbee, E., Lee, J. E., Dubey, M., Dooley, J. F., Shuck, C., Minschwaner, K., Santos, A., Biraud, S., and Dubey, M. K.: Gaussian Plume Methane Flux Inversions from a Super-emitting Orphan Well using Ambient Observations to Prioritize Plugging and Carbon Credits, [https://docs.google.com/document/d/1EsnYlbtFWQ2WrH1nxYNH40dsFIIO-DiR\\_\\_ju8Eyd4Es/edit?usp=drive\\_link](https://docs.google.com/document/d/1EsnYlbtFWQ2WrH1nxYNH40dsFIIO-DiR__ju8Eyd4Es/edit?usp=drive_link), 2024.
- Frankenberg, C., Meirink, J. F., Van Weele, M., Platt, U., and Wagner, T.: Assessing Methane Emissions from Global Space-Borne Observations, *Science*, 308, 1010–1014, <https://doi.org/10.1126/science.1106644>, 2005.
- 650 Frankenberg, C., Thorpe, A. K., Thompson, D. R., Hulley, G., Kort, E. A., Vance, N., Borchardt, J., Krings, T., Gerilowski, K., Sweeney, C., Conley, S., Bue, B. D., Aubrey, A. D., Hook, S., and Green, R. O.: Airborne methane remote measurements reveal heavy-tail flux distribution in Four Corners region, *Proceedings of the National Academy of Sciences*, 113, 9734–9739, <https://doi.org/10.1073/pnas.1605617113>, 2016.
- Gålfalk, M., Nilsson Pålédal, S., and Bastviken, D.: Sensitive Drone Mapping of Methane Emissions without the Need for Supplementary Ground-Based Measurements, *American Chemical Society: Earth and Space Chemistry*, 5, 2668–2676, <https://doi.org/10.1021/acsearthspacechem.1c00106>, 2021.
- 655 Gisi, M., Hase, F., Dohe, S., Blumenstock, T., Simon, A., and Keens, A.: XCO<sub>2</sub>-measurements with a tabletop FTS using solar absorption spectroscopy, *Atmospheric Measurement Techniques*, 5, 2969–2980, <https://doi.org/10.5194/amt-5-2969-2012>, 2012.
- Glasby, G. P.: Abiogenic Origin of Hydrocarbons: An Historical Overview, *Resource Geology*, 56, 83–96, <https://doi.org/10.1111/j.1751-3928.2006.tb00271.x>, 2006.
- 660 Hansen, J., Sato, M., Ruedy, R., Lacis, A., and Oinas, V.: Global warming in the twenty-first century: An alternative scenario, *Proceedings of the National Academy of Sciences*, 2000.
- Heath, G., Warner, E., Steinberg, D., and Brandt, A.: Estimating U.S. Methane Emissions from the Natural Gas Supply Chain. Approaches, Uncertainties, Current Estimates, and Future Studies, Tech. Rep. NREL/TP-6A50-62820, 1226158, Joint Institute for Strategic Energy Analysis, <http://www.osti.gov/servlets/purl/1226158/>, 2015.
- 665 Heerah, S., Frausto-Vicencio, I., Jeong, S., Marklein, A. R., Ding, Y., Meyer, A. G., Parker, H. A., Fischer, M. L., Franklin, J. E., Hopkins, F. M., and Dubey, M.: Dairy Methane Emissions in California's San Joaquin Valley Inferred With Ground-Based Remote Sensing Observations in the Summer and Winter, *Journal of Geophysical Research: Atmospheres*, 126, e2021JD034785, <https://doi.org/10.1029/2021JD034785>, 2021.
- Hiller, R. V., Neiningner, B., Brunner, D., Gerbig, C., Bretscher, D., Künzle, T., Buchmann, N., and Eugster, W.: Aircraft-based CH<sub>4</sub> flux estimates for validation of emissions from an agriculturally dominated area in Switzerland, *Journal of Geophysical Research: Atmospheres*, 119, 4874–4887, <https://doi.org/10.1002/2013JD020918>, 2014.
- 670 Hodnebrog, Ø., Dalsøren, S. B., and Myhre, G.: Lifetimes, direct and indirect radiative forcing, and global warming potentials of ethane (C<sub>2</sub>H<sub>6</sub>), propane (C<sub>3</sub>H<sub>8</sub>), and butane (C<sub>4</sub>H<sub>10</sub>), *Atmospheric Science Letters*, 19, e804, <https://doi.org/10.1002/asl.804>, 2018.
- Hollenbeck, D., Nunez, G., Christensen, L. E., and Chen, Y.: Wind Measurement and Estimation with Small Unmanned Aerial Systems (sUAS) Using On-Board Mini Ultrasonic Anemometers, in: 2018 International Conference on Unmanned Aircraft Systems (ICUAS), pp. 285–292, IEEE, Dallas, TX, ISBN 978-1-5386-1354-2, <https://doi.org/10.1109/ICUAS.2018.8453418>, 2018.
- 675 Holmes, C. D., Prather, M. J., Søvde, O. A., and Myhre, G.: Future methane, hydroxyl, and their uncertainties: key climate and emission parameters for future predictions, *Atmospheric Chemistry and Physics*, 13, 285–302, <https://doi.org/10.5194/acp-13-285-2013>, 2013.



- Jacob, D. J., Varon, D. J., Cusworth, D. H., Dennison, P. E., Frankenberg, C., Gautam, R., Guanter, L., Kelley, J., McKeever, J., Ott, L. E., Poulter, B., Qu, Z., Thorpe, A. K., Worden, J. R., and Duren, R. M.: Quantifying methane emissions from the global scale down to point sources using satellite observations of atmospheric methane, *Atmospheric Chemistry and Physics*, 22, 9617–9646, <https://doi.org/10.5194/acp-22-9617-2022>, 2022.
- Johnson, D., Heltzel, R., and Oliver, D.: Temporal Variations in Methane Emissions from an Unconventional Well Site, *American Chemical Society: Omega*, 4, 3708–3715, <https://doi.org/10.1021/acsomega.8b03246>, 2019.
- Karion, A., Sweeney, C., Pétron, G., Frost, G., Michael Hardesty, R., Kofler, J., Miller, B. R., Newberger, T., Wolter, S., Banta, R., Brewer, A., Dlugokencky, E., Lang, P., Montzka, S. A., Schnell, R., Tans, P., Trainer, M., Zamora, R., and Conley, S.: Methane emissions estimate from airborne measurements over a western United States natural gas field, *Geophysical Research Letters*, 40, 4393–4397, <https://doi.org/10.1002/grl.50811>, 2013.
- Karion, A., Sweeney, C., Kort, E. A., Shepson, P. B., Brewer, A., Cambaliza, M., Conley, S. A., Davis, K., Deng, A., Hardesty, M., Herndon, S. C., Lauvaux, T., Lavoie, T., Lyon, D., Newberger, T., Pétron, G., Rella, C., Smith, M., Wolter, S., Yacovitch, T. I., and Tans, P.: Aircraft-Based Estimate of Total Methane Emissions from the Barnett Shale Region, *Environmental Science & Technology*, 49, 8124–8131, <https://doi.org/10.1021/acs.est.5b00217>, 2015.
- Kort, E. A., Frankenberg, C., Costigan, K. R., Lindenmaier, R., Dubey, M. K., and Wunch, D.: Four corners: The largest US methane anomaly viewed from space, *Geophysical Research Letters*, 41, 6898–6903, <https://doi.org/10.1002/2014GL061503>, 2014.
- Kutcherov, V. G. and Krayushkin, V. A.: Deep-seated abiogenic origin of petroleum: From geological assessment to physical theory, *Reviews of Geophysics*, 48, RG1001, <https://doi.org/10.1029/2008RG000270>, 2010.
- Lan, X., Talbot, R., Laine, P., and Torres, A.: Characterizing Fugitive Methane Emissions in the Barnett Shale Area Using a Mobile Laboratory, *Environ Science & Technology*, <https://doi.org/10.1021/es5063055>, 2015.
- Lavoie, T. N., Shepson, P. B., Cambaliza, M. O. L., Stirm, B. H., Karion, A., Sweeney, C., Yacovitch, T. I., Herndon, S. C., Lan, X., and Lyon, D.: Aircraft-Based Measurements of Point Source Methane Emissions in the Barnett Shale Basin, *Environmental Science & Technology*, 49, 7904–7913, <https://doi.org/10.1021/acs.est.5b00410>, 2015.
- Lavoie, T. N., Shepson, P. B., Cambaliza, M. O. L., Stirm, B. H., Conley, S., Mehrotra, S., Faloona, I. C., and Lyon, D.: Spatiotemporal Variability of Methane Emissions at Oil and Natural Gas Operations in the Eagle Ford Basin, *Environmental Science & Technology*, 51, 8001–8009, <https://doi.org/10.1021/acs.est.7b00814>, 2017.
- Masson-Delmotte, V., Zhai, P., Pirani, A., Connors, S., Péan, C., Berger, S., Caud, N., Chen, Y., Goldfarb, L., Gomis, M., Huang, M., Leitzell, K., Lonnoy, E., Matthews, J., Maycock, T., Yu, R., and Zhou, B.: Climate Change 2021: The Physical Science Basis. Contribution of Working Group I to the Sixth Assessment Report of the Intergovernmental Panel on Climate Change, Cambridge University Press, 1 edn., ISBN 978-1-00-915789-6, <https://www.cambridge.org/core/product/identifier/9781009157896/type/book>, 2023.
- McKinney, K. A., Wang, D., Ye, J., De Fouchier, J.-B., Guimarães, P. C., Batista, C. E., Souza, R. A. F., Alves, E. G., Gu, D., Guenther, A. B., and Martin, S. T.: A sampler for atmospheric volatile organic compounds by copter unmanned aerial vehicles, *Atmospheric Measurement Techniques*, 12, 3123–3135, <https://doi.org/10.5194/amt-12-3123-2019>, 2019.
- Meyer, A. G., Lindenmaier, R., Heerah, S., Benedict, K. B., Kort, E. A., Peischl, J., and Dubey, M. K.: Using Multiscale Ethane/Methane Observations to Attribute Coal Mine Vent Emissions in the San Juan Basin From 2013 to 2021, *Journal of Geophysical Research: Atmospheres*, 127, e2022JD037092, <https://doi.org/10.1029/2022JD037092>, 2022.

- 715 Olaguer, E. P., Jeltema, S., Gauthier, T., Jermalowicz, D., Ostaszewski, A., Batterman, S., Xia, T., Ranases, J., Kovalchick, M., Miller, S., Acevedo, J., Lamb, J., Benya, J., Wendling, A., and Zhu, J.: Landfill Emissions of Methane Inferred from Unmanned Aerial Vehicle and Mobile Ground Measurements, *Atmosphere*, 13, 983, <https://doi.org/10.3390/atmos13060983>, 2022.
- Parker, R., Boesch, H., Cogan, A., Fraser, A., Feng, L., Palmer, P. I., Messerschmidt, J., Deutscher, N., Griffith, D. W. T., Notholt, J., Wennberg, P. O., and Wunch, D.: Methane observations from the Greenhouse Gases Observing SATellite: Comparison to ground-based  
720 TCCON data and model calculations, *Geophysical Research Letters*, 38, 2011GL047871, <https://doi.org/10.1029/2011GL047871>, 2011.
- Peischl, J., Eilerman, S. J., Neuman, J. A., Aikin, K. C., De Gouw, J., Gilman, J. B., Herndon, S. C., Nadkarni, R., Trainer, M., Warneke, C., and Ryerson, T. B.: Quantifying Methane and Ethane Emissions to the Atmosphere From Central and Western U.S. Oil and Natural Gas Production Regions, *Journal of Geophysical Research: Atmospheres*, 123, 7725–7740, <https://doi.org/10.1029/2018JD028622>, 2018.
- Pétron, G., Miller, B., Vaughn, B., Thorley, E., Kofler, J., Mielke-Maday, I., Sherwood, O., Dlugokencky, E., Hall, B., Schwietzke, S., Conley,  
725 S., Peischl, J., Lang, P., Moglia, E., Crotwell, M., Crotwell, A., Sweeney, C., Newberger, T., Wolter, S., Kitzis, D., Bianco, L., King, C., Coleman, T., White, A., Rhodes, M., Tans, P., and Schnell, R.: Investigating large methane enhancements in the U.S. San Juan Basin, *Elementa: Science of the Anthropocene*, 8, 038, <https://doi.org/10.1525/elementa.038>, 2020.
- Saad, K. M., Wunch, D., Toon, G. C., Bernath, P., Boone, C., Connor, B., Deutscher, N. M., Griffith, D. W. T., Kivi, R., Notholt, J., Roehl, C., Schneider, M., Sherlock, V., and Wennberg, P. O.: Derivation of tropospheric methane from TCCON CH<sub>4</sub> and HF total column  
730 observations, preprint, *Gases/Remote Sensing/Data Processing and Information Retrieval*, <https://amt.copernicus.org/preprints/7/3471/2014/amtd-7-3471-2014.pdf>, 2014.
- Scherer, J. J.: Next-Generation Laser-Based Natural Gas Leak Detection, 2017.
- Schneising, O., Buchwitz, M., Reuter, M., Vanselow, S., Bovensmann, H., and Burrows, J. P.: Remote sensing of methane leakage from natural gas and petroleum systems revisited, *Atmospheric Chemistry and Physics*, 20, 9169–9182, <https://doi.org/10.5194/acp-20-9169-2020>, 2020.  
735
- Schwietzke, S., Pétron, G., Conley, S., Pickering, C., Mielke-Maday, I., Dlugokencky, E. J., Tans, P. P., Vaughn, T., Bell, C., Zimmerle, D., Wolter, S., King, C. W., White, A. B., Coleman, T., Bianco, L., and Schnell, R. C.: Improved Mechanistic Understanding of Natural Gas Methane Emissions from Spatially Resolved Aircraft Measurements, *Environmental Science & Technology*, 51, 7286–7294, <https://doi.org/10.1021/acs.est.7b01810>, 2017.
- 740 Seinfeld, J. H. and Pandis, S. N.: *Atmospheric Chemistry and Physics: From Air Pollution to Climate Change*, Wiley-Interscience, 2nd edn., ISBN 978-0-471-72018-8, 2006.
- Shah, A., Allen, G., Pitt, J. R., Ricketts, H., Williams, P. I., Helmore, J., Finlayson, A., Robinson, R., Kabbabe, K., Hollingsworth, P., Rees-White, T. C., Beaven, R., Scheutz, C., and Bourn, M.: A Near-Field Gaussian Plume Inversion Flux Quantification Method, Applied to Unmanned Aerial Vehicle Sampling, *Atmosphere*, 10, 396, <https://doi.org/10.3390/atmos10070396>, 2019.
- 745 Sherwin, E., El Abbadi, S., Burdeau, P., Zhang, Z., Chen, Z., Rutherford, J., Chen, Y., and Brandt, A.: Single-blind test of nine methane-sensing satellite systems from three continents, preprint, *Atmospheric Sciences*, <https://eartharxiv.org/repository/view/5605/>, 2023.
- Simpson, I. J., Sulbaek Andersen, M. P., Meinardi, S., Bruhwiler, L., Blake, N. J., Helmig, D., Rowland, F. S., and Blake, D. R.: Long-term decline of global atmospheric ethane concentrations and implications for methane, *Nature*, 488, 490–494, <https://doi.org/10.1038/nature11342>, 2012.
- 750 Solomon, S., Qin, D., Manning, M., Chen, Z., Marquis, M., Averyt, K., Tignor, M., and Miller, H.: *Climate Change 2007: The Physical Science Basis. Contribution of Working Group I to the Fourth Assessment Report of the Intergovernmental Panel on Climate Change*, Cambridge University Press, Cambridge, ISBN 978-0-521-88009-1 978-0-521-70596-7, 2007.

- Song, C., Zhu, J.-J., Willis, J. L., Moore, D. P., Zondlo, M. A., and Ren, Z. J.: Methane Emissions from Municipal Wastewater Collection and Treatment Systems, *Environmental Science & Technology*, 57, 2248–2261, <https://doi.org/10.1021/acs.est.2c04388>, 2023.
- 755 Space Studies Board, Division on Engineering and Physical Sciences, and National Academies of Sciences, Engineering, and Medicine: Thriving on Our Changing Planet: A Decadal Strategy for Earth Observation from Space: An Overview for Decision Makers and the Public, National Academies Press, Washington, D.C., ISBN 978-0-309-49241-6, <https://www.nap.edu/catalog/25437>, 2019.
- Stockie, J. M.: The Mathematics of Atmospheric Dispersion Modelling, *Society for Industrial and Applied Mathematics Review*, pp. 349–372, 2011.
- 760 Stolper, D. A., Lawson, M., Formolo, M. J., Davis, C. L., Douglas, P. M. J., and Eiler, J. M.: The utility of methane clumped isotopes to constrain the origins of methane in natural gas accumulations, *Geological Society, London, Special Publications*, 468, 23–52, <https://doi.org/10.1144/SP468.3>, 2018.
- Taylor, J. R.: *An Introduction to Error Analysis: The Study of Uncertainties in Physical Measurements*, University Science Books, 2nd edn., ISBN 978-0-935702-75-0, 1996.
- 765 Travis, B., Dubey, M., and Sauer, J.: Neural networks to locate and quantify fugitive natural gas leaks for a MIR detection system, *Atmospheric Environment: X*, 8, 100 092, <https://doi.org/10.1016/j.aeaoa.2020.100092>, 2020.
- Turner, A. J., Jacob, D. J., Wecht, K. J., Maasakkers, J. D., Lundgren, E., Andrews, A. E., Biraud, S. C., Boesch, H., Bowman, K. W., Deutscher, N. M., Dubey, M. K., Griffith, D. W. T., Hase, F., Kuze, A., Notholt, J., Ohyama, H., Parker, R., Payne, V. H., Sussmann, R., Sweeney, C., Velazco, V. A., Warneke, T., Wennberg, P. O., and Wunch, D.: Estimating global and North American methane emissions with high spatial resolution using GOSAT satellite data, *Atmospheric Chemistry and Physics*, 15, 7049–7069, <https://doi.org/10.5194/acp-15-7049-2015>, 2015.
- 770 Vaughn, T. L., Bell, C. S., Pickering, C. K., Schwietzke, S., Heath, G. A., Pétron, G., Zimmerle, D. J., Schnell, R. C., and Nummedal, D.: Temporal variability largely explains top-down/bottom-up difference in methane emission estimates from a natural gas production region, *Proceedings of the National Academy of Sciences*, 115, 11 712–11 717, <https://doi.org/10.1073/pnas.1805687115>, 2018.
- 775 Viatte, C., Lauvaux, T., Hedelius, J. K., Parker, H., Chen, J., Jones, T., Franklin, J. E., Deng, A. J., Gaudet, B., Verhulst, K., Duren, R., Wunch, D., Roehl, C., Dubey, M. K., Wofsy, S., and Wennberg, P. O.: Methane emissions from dairies in the Los Angeles Basin, *Atmospheric Chemistry and Physics*, 17, 7509–7528, <https://doi.org/10.5194/acp-17-7509-2017>, 2017.
- Villa, T., Gonzalez, F., Miljevic, B., Ristovski, Z., and Morawska, L.: An Overview of Small Unmanned Aerial Vehicles for Air Quality Measurements: Present Applications and Future Prospectives, *Sensors*, 16, 1072, <https://doi.org/10.3390/s16071072>, 2016.
- 780 Woodward, J. L.: Estimating the flammable mass of a vapor cloud, *A CCPS concept book*, Center for Chemical Process Safety of the American Institute of Chemical Engineers, New York, N.Y, ISBN 978-0-8169-0778-6, 1998.